Title: FMRP controls diacylglycerol-dependent neuronal activity by mediating m^6A-regulated translation efficiency

Authors: Oktay Cakil[1], Boglarka Zambo[1], Tatiana, Maroilley[1], Nathalie Drouot[1], Anastasiya Petrova[1], Luc Negroni[1], Gergo Gogl[1], Amélie Piton[1,2] & Hervé Moine[1*]

Affilitations:

1. Institut de Génétique et de Biologie Moléculaire et Cellulaire (IGBMC), Centre National de la Recherche Scientifique (CNRS UMR7104), Institut National de la Santé et de la Recherche Médicale (INSERM U1258), Université de Strasbourg, Illkirch 67400, France
2. Unité de Génétique Moléculaire, IGMA, Hôpitaux Universitaire de Strasbourg, Strasbourg, France

*Address for correspondence and material request:

Hervé Moine, Laboratoire "Mécanismes génétiques des maladies neurodéveloppementales", IGBMC, 1 rue Laurent Fries, 67400 Illkirch, France

Tel : +33 3 88 65 56 78

E-mail: moine@igbmc.fr

Abstract

Fragile X syndrome (FXS), the most common inherited form of intellectual disability and autism, arises from loss of the RNA-binding protein FMRP. How FMRP loss disrupts neuronal proteostasis remains incompletely understood. Here we identify diacylglycerol kinase kappa (DGKκ) as a principal FMRP mRNA target across the brain. FMRP deficiency markedly reduces neuronal DGKκ, and selective DGKκ loss recapitulates key FXS phenotypes, including hyperactivity and compulsive behaviors, aberrant dendritic spine morphology, and elevated translation. Mechanistically, FMRP binds repetitive DGKκ RNA motifs enriched in N6-methyladenosine (m^6A) modifications. These interactions relieve a translational blockade imposed by the encoded amino acid composition, thereby enhancing DGKκ synthesis. Our findings establish DGKκ as a critical mediator of FMRP function and reveal a general mechanism by which FMRP couples m^6A-modified, codon-biased sequences to efficient translation. This work uncovers a regulatory axis linking RNA modification, codon usage, and neuronal proteostasis, illuminating new principles of translational control in neurodevelopmental disorders.

Introduction

Fragile X syndrome (FXS) is one of the most frequent monogenic causes of intellectual disability (ID) and autism spectrum disorders (ASD). FXS has a prevalence of about 1:5000 males and 1:8000 females and is associated with comorbidities including hyperactivity, anxiety, hypersensitivity, stereotypies, epilepsy, connective tissue dysplasia, macro-orchidism and facial dysmorphism (Hagerman et al., 2017). FXS is caused by the loss of expression or function of the *FMR1* gene encoding FMRP, an RNA binding protein proposed to have diverse functions, including the regulation of the translation of mRNAs important for synaptic plasticity (Darnell and Klann, 2013). The *Fmr1*-KO mouse ("*Fmr1* Knockout Mice," 1994) recapitulates FXS-like phenotypes and revealed that FMRP loss leads to alterations of several G protein-coupled receptor signaling pathways, notably the overactivation of group 1 metabotropic glutamate receptor (mGluRI) signaling (Bear et al., 2004) associated to neuronal translation excess and abnormal dendritic spine morphology in several areas of the brain (Qin et al., 2005; Dölen et al., 2007). These alterations are proposed to account, at least in part, for the behavioral alterations of the *Fmr1*-KO model. The mechanism by which the loss of FMRP leads to these alterations is however not clearly established. A prevailing model states that the abnormal mGluRI signaling and excessive translation in FXS condition is the result of a lack of repression by FMRP of some specific mRNA targets involved in mGluR1/5 signaling (Bear et al., 2004). While studies suggested that FMRP associates with mRNAs on a transcriptome-wide scale via short sequence abundant motifs (Ascano et al., 2012; Maurin et al., 2018), other studies have identified specific mRNAs bound via more complex less frequent motifs (Darnell et al., 2001; Schaeffer et al., 2001; Bechara et al., 2009), making the selection mechanism of mRNAs by FMRP and its overall impact on neuronal translatome unclear.

The diacylglycerol kinase kappa (DGKκ) mRNA was evidenced as an mRNA most co-immunoprecipitated with FMRP in a CLIP (cross-linking and immunoprecipitation) assay performed in primary murine cortical neurons (Tabet et al., 2016a; Habbas et al., 2022). Together with the fact that purified FMRP binds DGKκ mRNA with unprecedent affinity compared to other proposed targets, this suggested that DGKκ might be a prominent target of FMRP and thus an important player in FXS (Tabet et al., 2016a). DGKκ protein level was found severely reduced in *Fmr1*-KO mouse and FXS brain extracts while its RNA level was unaffected (Tabet et al., 2016a; Habbas et al., 2022), indicating that FMRP is required for the translation of DGKκ, in apparent contradiction with its primarily described function as a translation repressor (Li et al., 2001). DGKκ could play an important role in FXS because it is a modulator of diacylglycerol (DAG) and phosphatidic acid (PA), two second messenger lipids playing a pivotal role in protein synthesis control and spine morphology dynamics (Tabet et al., 2016b; Moine and Vitale, 2019) and involved in the signaling of several GPCR-coupled pathways altered in FXS. In agreement with a role in neuronal DAG signaling, FMRP loss disrupts mGluRI-dependent DAG signaling (Tabet et al., 2016a). Moreover, treatment of young adult *Fmr1*-KO mice with adeno-associated viral (AAV) vectors expressing a modified FMRP-independent DGKκ transgene provided long-term correction of the cerebral DAG/PA unbalance and of the FXS-related core behavioral phenotypes (Habbas et al., 2022). These data underscored that DGKκ loss could be a main contributor to FXS pathomechanism, but the exact contribution of DGKκ in neuronal function and the mechanism by which FMRP controls DGKκ expression were however unknown.

Here we have characterized the biological impact of the lack of DGKκ and investigated why FMRP is necessary for DGKκ translation. Using a mouse model of DGKκ knock-down we demonstrate that DGKκ activity controls neuronal translation in correlation with neuron

signaling, neuron morphology, and behavioral alteration, reminiscent of the function of FMRP itself. We demonstrate that *Dgkk* mRNA is a favored FMRP target in different neuronal subtypes via its binding to a uniquely repeated consensus sequence that encodes non-optimal codons. We evidence the requirement of m^6A RNA modifications for attracting FMRP together with other factors including FXRs and enabling the translation of a ribosome collision prone sequence within DGKκ mRNA. Finally, we evidence that FMRP globally associates with RNA sequences encoding repeated amino acids reducing translation efficiency.

Overall, this study sheds light on a novel contribution of FMRP to facilitate translation of a master regulator playing a key role in neurological functions and FXS pathology.

Results

Dgkk mRNA is a favoured target of FMRP and FXR proteins in several neuronal subtypes

We previously demonstrated by crosslinking immunoprecipitation (CLIP) microarray that *Dgkk* mRNA is a primary target of FMRP in primary cortical neurons (Tabet et al., 2016a). The heterogeneous pattern of expression of *Dgkk* in the brain (**Fig. 1A**) and its neuronal specific expression (**Fig. 1B**) prompted us to determine whether the interaction between FMRP and *Dgkk* mRNA was conserved across different brain regions. Thus, using our validated CLIP approach (Tabet et al., 2016a) (**Supplemental Figure S1A**) we compared FMRP interaction in cortical neurons, where DGKκ expression is very low, and in hypothalamic neurons, where *Dgkk* is over 40-fold higher (**Fig. 1C**). CLIP-qRT-PCR analyses revealed a strong and specific enrichment of *Dgkk* mRNA relative to input similar in both neuron subtypes (**Fig. 1D, E**). This suggests that *Dgkk* mRNA is a favored target of FMRP compared with other proposed targets such as *Map1b* and *Psd95*, across different brain

regions. *Dgkk* mRNA level is not affected by FMRP loss in the brain (**Fig. 1F**). To assess the consequence of FMRP loss on DGKκ protein level, we used targeted proteomic strategy Parallel Reaction Monitoring mass spectrometry combined with stable isotope-labeled standard peptides (PRM-SIS) to assess DGKκ absolute level. An 80% reduction in DGKκ protein level was observed in *Fmr1*-KO cortical neurons (initial cell type where FMRP-*Dgkk* interaction was discovered) contrasting with a nearly 50% decrease observed in the hypothalamus (where DGKκ is most expressed) (**Fig. 1G**).

Interestingly, FXRs expression pattern diverge throughout the brain. *Fmr1* exhibits higher expression level in the cortex than in the hypothalamus, contrasting with *Fxr1p* which shows the opposite (**Supplemental Figure S1B**). We corroborated this observation at the protein level on adult mouse cortex and hypothalamus, revealing a reciprocal expression of FMRP and FXR1P in both brain regions, with FMRP being approximately 4-fold more expressed in the cortex than in the hypothalamus, and FXR1P around 2-fold more expressed in the hypothalamus than in the cortex (**Fig. 1H**).

The FXR proteins (FMRP, FXR1P, and FXR2P) exhibit approximately 65% homology in mammals (Siomi et al., 1996), each possessing well-conserved RNA binding domains, namely KH1, KH2, and RGG. FXR1P and FXR2P are postulated to exhibit functional redundancy, partially overlapping with FMRP.

To test whether other FXRs have the ability to bind and regulate *Dgkk* mRNA, we employed a CLIP-qRT-PCR approach targeting FXR1P in primary hypothalamic neurons where the *Dgkk* expression is the highest. A significant enrichment of *cMyc mRNA*, a previously proposed target of FXR1P (George et al., 2021), was observed relative to input and IgG when compared to the negative control *Rplp0*. In contrast, *Dgkk* mRNA exhibited over 5 to 10-fold higher enrichment compared to all the mRNA targets tested (including *Map1b*, *cMyc*, *Psd95*) (**Fig. 1I**).

Together, these findings support a model of functional redundancy among FXR proteins in the regulation of DGKκ expression and identify *Dgkk* as an atypical candidate gene for FXS characterized by its FXR-dependent expression.

Loss of *Dgkk* in mouse leads to hyperactivity and compulsive-like behavior associated with an overgrowth phenotype

To assess the biological role of DGKκ, a DGKκ knockout mouse (*Dgkk*-KO) was generated by deleting its critical exon 8 using CRISPR-Cas9 technology, leading to a frameshift and premature stop codon in exon 9. The knockout allele was verified through qRT-PCR verification of the exon 8 deletion (**Supplemental Figure S2A**). Detection of DGKκ by conventional methods is challenging due to its low protein abundance and the absence of specific commercial antibodies (**Supplemental Figure S2B**). Using PRM-SIS-MS to quantify DGKκ levels, we effectively measured low level of DGKκ in WT brain samples and confirmed its absence in the *Dgkk*-KO mouse model (**Supplemental Figure S2CD**). Moreover, no genetic compensation was observed with the 9 other DGK genes suggesting the absence of transcriptional interdependency of *Dgkk* and the other DGKs (**Supplemental Figure S2E**). Mice lacking DGKκ did not exhibit an overt phenotype and no reproduction bias was noted. General morphological observation revealed no significant congenital malformation differences between *Dgkk*-KO and its WT littermates. Notably, we did not observe abnormal penis development (**Supplemental Figure S2F**), in contrast with previous GWAS study suggesting the involvement of DGKκ in hypospadias, a male developmental condition where urethra closure is abnormal (van der Zanden et al., 2011), but in agreement with a recent genetic study (Richard et al., 2019). At 13 weeks of age, both WT and *Dgkk*-KO mice underwent a battery of behavioral tests. Use of open field test revealed an increased locomotor activity of *Dgkk*-KO compared to WT mice with increased time spent in the center

of the arena (**Fig. 2A**) that were evocative of a hyperactivity behavior and/or reduced anxiety. A tendency for hyperactivity was also supported by the increased marble burying (**Fig. 2B**). Increased digging duration and number of diggings suggested compulsive-like behavior (**Fig. 2B**). An increased contact numbers and duration in the social interaction test suggested increased sociability, but could also resulted from hyperactivity and reduced anxiety (**Fig. 2C**). Increased time in the open arm in the elevated plus maze with increased arm entries trends suggested also hyperactivity and reduced anxiety (**Supplemental Figure S2G-J**). A trend for alteration of recognition ability was observed in the novel object recognition test (**Supplemental Figure S2 K-M**), suggesting *Dgkk*-KO mice do not present major episodic-like memory alteration. No nesting behavior defect was detected (**Supplemental Figure S2N**). Finally, the startle response amplitude after pre-pulse Inhibition (PPI) was also found significantly increased (**Fig. 2D**), suggesting that *Dgkk*-KO mice have a sensorimotor gating deficit and a hypersensitivity to acoustic stimuli. These findings collectively underscored the impact of DGKκ loss on various aspects of mouse cognitive behavior, highlighting its role in neurodevelopment. Morphological alterations are frequent comorbidities of intellectual developmental disorders. The *Fmr1*-KO mouse model for instance exhibits various physiological alterations (The Dutch-Belgian Fragile X Consortium, 1994; Leboucher et al., 2019). Investigating whether similar changes occur in the *Dgkk*-KO mouse model, we observed a progressive increase in body weight from 3 weeks to 22 weeks of age (**Fig. 2E**). Further analyses using qNMR (quantitative nuclear magnetic resonance) revealed that the weight gain was not attributable to an increased size (**Fig. 2F**) or an accumulation of fat (**Fig. 2G**) but rather to an increase in lean body mass (**Fig. 2H**) and free body fluid (**Fig. 2I**). Meanwhile, bone density was significantly increased (**Fig. 2J**). We also measured an increased heart weight (**Fig. 2K**) associated with an increase in the left ventricle mass (**Fig. 2L**).

Functionally, the *Dgkk*-KO heart showed no significant heart failures despite an increase in blood volume in the left ventricle during both diastole and systole, suggesting a compensatory mechanism (**Supplemental Figure S2OP**).

Overall, the *Dgkk*-KO mouse model exhibits a peculiar overgrowth phenotype associated with hyperactivity, hypersensitivity and compulsive-like behavior indicating that loss of DGKκ leads to syndromal neuronal and non-neuronal developmental defects.

Loss of DGKκ alters dendritic spine morphology and mGluRI-dependent activity and leads to excessive neuronal translation

Among the 10 DGK isoenzymes, DGKκ exhibits the lowest global expression and is uniquely expressed in the brain, according to the human protein atlas database (https://www.proteinatlas.org/). The neuron-specific expression of DGKκ (**Fig 1B**) and the neurodevelopmental behavioral alterations caused by its depletion suggested that DGKκ plays important neuronal functions. To identify the neuronal subcellular localization of DGKκ, we conducted an overexpression experiment in primary neurons and performed immunostaining against HA-tagged DGKκ at DIV17. DGKκ was predominantly found enriched at the plasma membrane, similar to when it was overexpressed in non-neuronal cells (Imai et al., 2005). Within dendrites, DGKκ was found specifically enriched in post-synaptic densities of mature spines colocalizing with the synaptic marker PSD95 (**Fig. 3A**) and ribopuromycylation signal (**Fig. 3B and Supplemental Figure S3A**). This finding supports a role of DGKκ in synaptic function and suggests a contribution in modulating dendritic spines local translation.

Dendritic spine morphology is frequently altered in neurodevelopmental disorders and these morphological alterations are proposed as an underlying cause of these disorders (He and Portera-Cailliau, 2013). To analyze the effects of DGKκ loss on dendritic spine morphology, primary hippocampal neurons from WT and *Dgkk*-KO mice were magnetofected at 4DIV

with a GFP-expressing plasmid and imaged at DIV21. A significant decrease in mature "stubby" and "mushroom" spines alongside a notable increase in immature "long thin" and "filopodia" spines was observed in *Dgkk*-KO neurons (**Fig. 3C**).

Given the cognitive alterations of *Dgkk*-KO mice, the increased proportion of immature spines in *Dgkk*-KO neurons, and the consequences of other DGKs loss on synaptic plasticity (Lee et al., 2016a), we hypothesized that the loss of DGKκ would likely lead to synaptic transmission dysfunction. To test this hypothesis, we recorded the neuronal activity of WT and *Dgkk*-KO primary cortical neurons at DIV21 (time at which neural activity was highest **Supplemental Figure S3B**)

on high-density multi-electrode array (HD-MEA) chips. The maturity of the culture was assessed by the spiking frequency of individual neurons, the burst neuronal network activity (**Supplemental Figure S3C**), and the responsiveness to (S)-3,5-Dihydroxyphenylglycine (DHPG), a specific agonist of group 1 metabotropic glutamate receptors (mGluRIs) (**Fig. 3D**). While the number of active units was consistent between WT and *Dgkk*-KO neurons, reflecting a comparable number of cells on the HD-MEA chip, at basal level, we observed similar firing rates and burst network frequencies between WT and *Dgkk*-KO neurons, suggesting no apparent difference in absence of stimuli (**Fig. 3D**). However, upon neuronal activation with DHPG, we observed a 5-fold increase in neuronal firing rate for WT neurons, compared to only a 3-fold increase for *Dgkk*-KO neurons. Furthermore, WT neurons showed an increased synchronization of their network activity whereas *Dgkk*-KO neurons showed a loss of synchronization (**Fig. 3D**). Overall, the absence of DGKκ in neurons disrupts their intrinsic firing activity and synaptic transmission, resulting in alterations to the neuronal network coherence in vitro.

DGKs convert DAG into PA and are thought to play a key role in neuronal signaling by attenuating DAG-mediated pathways (Lee et al., 2016). To define the molecular alterations

caused by the loss of DGKκ, we analyzed the activation status of several members of the DAG-activated pathways in cortical neurons. PKC, a main direct effector of DAG was found overactivated (**Fig. 3E**), in agreement with an excess of DAG signaling. Analysis of several other downstream effectors revealed that AKT, S6, and eIF4E were also overactivated, further supporting the alteration of DAG signaling. S6 and eIF4E are final effectors of DAG-mediated pathways, their phosphorylation levels in the brain are associated with enhanced protein synthesis rate (Kong and Lasko, 2012; Biever et al., 2015). Concordantly, neuronal translation rate was found to be increased in *Dgkk*-KO cortical neurons by puromycin incorporation assay (**Fig. 3F**). We further confirmed that DAG pathway was altered in hypothalamic primary neurons, as DGKκ is expressed at a much higher level in this neuronal type (**Supplemental Figure S3D**).

Together, these findings indicate that DGKκ deficiency leads to overactivation of mGluRI-DAG signaling pathways, resulting in elevated neuronal protein synthesis, likely because of impaired conversion of DAG to PA.

FMRP binds in an m^{6}A-dependent manner to RNA repeats that hamper translation

Identifying FMRP binding site on its RNA targets could help elucidate the mechanism(s) by which FMRP modulates translation. The G-quadruplex motif has been identified as the highest-affinity binding site to date (Darnell et al., 2001, 2004; Schaeffer et al., 2001; Suhl et al., 2014). However, our attempts to detect a G-quadruplex motif within *Dgkk* mRNA have been unsuccessful (Tabet et al., 2016a), suggesting that FMRP binds to a different type of motif in this mRNA. *Dgkk* exhibits low expression levels, which poses challenges for conventional CLIP-seq methods to achieve adequate coverage of this gene. To address this issue, we adopted a HITS-CLIP strategy in hypothalamic neurons to enhance sequencing coverage of *Dgkk*. The robustness of our HITS-CLIP approach was supported by the detection

of a single, well-defined FMRP-binding peak in the GC-rich exon 14 of *Fmr1* (**Supplemental Figure S4A**), the initial G-quadruplex–forming region with high affinity for FMRP, and by the lack of enrichment of housekeeping genes like *Rplp0* mRNA (**Supplemental Figure S4A**), together with a significant overlap with previous FMRP-CLIP studies (**Supplemental Figure S4B**). Strikingly, a single strong FMRP peak was identified in the *Dgkk* transcript, located within the coding sequence of exon 1 (**Fig. 4A**). This result was further confirmed using a modified iCLIP method (individual-nucleotide resolution UV crosslinking and immunoprecipitation) (Huppertz et al., 2014). The RNA crosslinked to FMRP was digested with proteinase K, generating small polypeptides cross-linked to RNA that can induce reverse transcription arrests (RT-stops) during cDNA synthesis, thereby allowing mapping of crosslink site. To improve the detection of RT-stop events across the *Dgkk* transcript, we designed 18 *Dgkk*-specific primers spaced approximately 100 nucleotides apart, ensuring uniform reverse transcription coverage. Using this method, RNA extracted from WT and *Fmr1*-KO immunoprecipitated samples, as well as input brain total RNA, underwent reverse transcription under identical conditions. This approach allowed us to identify WT-specific RT-stop events that were absent in both *Fmr1*-KO and input RNA samples (**Supplemental Figure S4C**).

The FMRP binding site on *Dgkk* mRNA spans a ~400-nucleotide region characterized by a high GC content and corresponds to more than 20 conserved repeats, preserved at both the RNA and protein levels, located downstream of a proline-rich region. The repetitive sequences are composed of a conserved GARCCGGCCCCA dodecamer motif (**Fig. 4A**) that encodes EPAP/EPDP amino acid repeats predicted to be intrinsically disordered (**Supplemental Figure S4D**). Interaction of FMRP with this sequence was confirmed by showing the interaction can be recapitulated on an exogenous RNA. Thus, a reporter (NLuc)

fused to the EPAP repeats is strongly bound by FMRP, compared with a control construct lacking this region (**Fig. 4B**).

While proline repeats are a well-established cause of ribosome pausing (Gutierrez et al., 2013), acidic amino acids-rich sequences (aspartate D and glutamate E) encoded by FMRP binding site in *Dgkk* have also been described to alter translation dynamics (Zhao et al., 2021; Ito et al., 2022; Aguilar Rangel et al., 2024). This suggest that the N-terminal region in exon 1 of *DGKκ* may negatively regulates its translation. To validate this hypothesis, we deleted the N-terminal region of DGKκ encompassing this sequence which resulted in a marked increase in DGKκ expression (**Fig. 4C**). Consistently, reporter construct containing the DGKκ N-terminal region (Nter-DGKκ-NLuc) displayed approximately sixfold lower expression than control construct, indicating that this region acts as a strong repressive element for DGKκ expression (**Supplemental Figure S4E**). Then, to distinguish the contributions of the RNA sequence itself from its role in protein coding, we introduced reading-frame shifts that altered the resulting polypeptide sequence while preserving the overall RNA sequence. As expected, disrupting the proline-rich motif increased NLuc activity, consistent with a relief of peptide-mediated translational repression. Strikingly, similar frame shifts within the EPAP domain produced a comparable increase in NLuc activity, indicating that the inhibitory effect of this region is primarily encoded in the codons sequence or the nascent peptide itself rather than at the RNA sequence level (**Supplemental Figure S4E**). Because impaired translation elongation promotes ribosomal collisions (Veltri et al., 2022), we next investigated whether the EPAP constituted a reading frame that promotes such collisions. To this end, we performed RNase protection assays to detect ribosome-protected RNA fragments within the DGKκ N-terminal region. Treatment of cells with a low concentration of the elongation inhibitor emetine, which enhances ribosomal collisions, increased the abundance of disomes in RNase A–digested lysates fractionated on a sucrose gradient. (**Fig. 4D**). Accordingly, using

a radiolabeled probe targeting the luciferase sequence, we detected disome footprints of ~60 nt upon emetine treatment, in contrast to the ~30 nt monosome footprints observed in control condition (**Fig. 4D**). Strikingly, fusion of the N-terminal region of DGKκ upstream the NLuc reporter resulted in a strong depletion of monosome within the luciferase sequence, consistent with a strong translational roadblock imposed by the DGKκ N-terminal region (**Fig. 4E**). Moreover, when using an EPAP-specific probe, we detected ribosome footprints corresponding to higher-order collided ribosomes. Importantly, this signal was dependent on the EPAP coding frame: changing the reading frame within the EPAP motif markedly reduced the abundance of higher-order collision footprints relative to monosome footprints (**Fig. 4E**) and slightly increase the downstream monosome signal within the luciferase sequence, thereby excluding a contribution from RNA secondary structure. Together, these data demonstrate that the EPAP-encoding N-terminal region of DGKκ promotes ribosomal collisions in a reading frame–dependent manner, consistent with a mechanism of translation repression.

Importantly, magnetofection of wild-type and *Fmr1*-KO neurons with the N-ter–DGKκ–NLuc reporter partially recapitulated FMRP-dependent translational control of this region, as evidenced by an approximately 40% decrease in luciferase activity in the absence of FMRP (**Fig. 4F**). Specific deletion of the EPAP repeats abolished this translational regulation. Similarly, frameshift mutations within the EPAP motif (−1/+1 and +1/−1), which preserve the RNA sequence while altering the encoded protein, also eliminated FMRP-dependent control (**Fig. 4F**). Notably, changing the reading frame within the proline-rich sequence produced a comparable loss of regulation, indicating that those elements within the encoded protein sequence, rather than the RNA sequence itself, are critical for mediating FMRP-dependent translational control (**Fig. 4F**).

Altogether, our data indicate that FMRP promotes translation efficiency in a context-dependent manner at sequences encoding repeated non-optimal amino acids.

A growing number of studies suggest that mRNAs bound by FMRP are enriched in m^6A modifications (Chang et al., 2017; Edens et al., 2019; Worpenberg et al., 2021; Zhang et al., 2022; Zou et al., 2023). We therefore investigated whether *Dgkk* mRNA contained m^6A modifications and sought to map their location within the transcript. Analysis of brain m^6A-seq datasets (Shafik et al., 2021) revealed a single m^6A peak on *Dgkk* mRNA, located in exon 1 (**Fig. 4A**). This localization contrasts with the typical m^6A distribution, which is predominantly found around the stop codon or in long internal exons (Murakami and Jaffrey, 2022). Notably, this m^6A peak exactly overlaps with the FMRP 'EPAP' binding site in exon 1 (**Fig. 4G**).

To determine whether m^6A modifications in *Dgkk* mRNA are required for FMRP binding, we performed CLIP-qRT-PCR experiments in primary cortical neurons where METTL3, the catalytic component of the METTL3/METTL14 m^6A writer complex, was silenced using siRNAs. We confirmed a nearly 50% reduction in *Mettl3* expression after 72 hours in neurons (**Supplemental Figure S4F**) and observed significant upregulation of *Psd95*, as well as a trend toward upregulation of *Dgkk*, *Cdk5r1*, and *Bdnf*, potentially attributable to the role of m^6A in mRNA decay (Lee et al., 2020) (**Supplemental Figure S4F**). We assessed the interaction between FMRP and several known FMRP mRNA targets containing m^6A modifications, including *Map1b*, *Psd95*, *Cdk5r1*, and *Dgkk*. We also included *Bdnf* (methylated) and *Rplp0* (unmethylated) mRNAs, which are not known FMRP targets, as controls. Strikingly, among all mRNAs tested, only *Dgkk* showed a significant reduction in CLIP efficiency upon *Mettl3* knockdown. Specifically, IP/Input enrichment decreased by approximately 50% in *Mettl3* knockdown conditions compared to controls (**Fig. 4G**), indicating that FMRP binding to *Dgkk* mRNA is dependent on m^6A modifications.

Recent studies suggest that FMRP directly binds to m^6A modifications within specific sequence contexts. Specifically, studies have shown that FMRP does not directly bind to the most common m^6A consensus motif, 'GGACU', but instead prefers motifs such as 'AGACU', and, albeit to a lesser extent, 'GAACU' (Zhang et al., 2022). Other research indicates that FMRP binding to m^6A may be mediated by m^6A reader proteins (Worpenberg et al., 2021). Notably, the mouse EPAP m^6A consensus motifs contain less common sequences, such as 11 GAACC, 7 GGACC, 7 AGACU, and 2 GAACU repeats.

To investigate whether FMRP binding to the EPAP motif is direct and dependent on m^6A, we analyzed the interaction of purified human FMRP isoform 1, the most abundant isoform, with a 76-nt synthetic RNA sequence containing 7 m^6A consensus sites derived from the original EPAP 400-nt sequence. Using EMSA, we confirmed a direct interaction between FMRP and the EPAP motif, with a twofold higher affinity for the methylated EPAP motif compared to the unmethylated motif (**Supplemental Figure S4H**). These findings indicate that FMRP can bind the EPAP motif *in vitro* and that its affinity is enhanced by m^6A modifications.

m^6A modifications recruit proteins that regulate RNA fate at various levels (Arguello et al., 2017; Edupuganti et al., 2017; Kan et al., 2021; Worpenberg et al., 2021; Zhang et al., 2022). Given that these proteins may influence the translational regulation of DGKκ by FMRP, we conducted RNA-pulldown proteomic analysis using biotinylated EPAP RNA probes, with and without m^6A modifications, immobilized on streptavidin beads and incubated with cortical neuronal lysate. We observed enrichment of FMRP, as well as its paralogs FXR1P and FXR2P, with the methylated probe (**Fig. 4H and Supplemental Table S1**), consistent with the EMSA and CLIP results. Additionally, we observed significant enrichment of the m^6A readers YTHDF1, YTHDF3, and to a lesser extent, YTHDF2 (**Fig. 4H**). The well-established m^6A readers YTHDC1 and YTHDC2, were not enriched with the m^6A-containing EPAP motif. Moreover, the stress granule factor G3BP1 exhibited a preference for the unmethylated

probe, as previously demonstrated (Edupuganti et al., 2017). Analysis of RIP-seq datasets from m^6A readers YTHDF1, YTHDF2, and YTHDF3 in primary hippocampal neurons (Flamand and Meyer, 2022) corroborated our RNA-pulldown results, with YTHDF1 and YTHDF3 showing higher binding affinity for *Dgkk* mRNA compared to YTHDF2 (**Supplemental Figure S4I**). We complemented these data using RNA native hold-up (RNA-nHU), an interactomic method adapted from (Zambo et al., 2022) that enables assessment of the relative binding affinities of an RNA ligand with its protein interactors within cell extracts (**Supplemental Figure S4J**). The RNA-nHU experiment was performed using both methylated and unmethylated EPAP bait probes at concentrations ranging from 0 to 2.5 µM, incubated with cortical neuronal lysate. First, we confirmed that YTHDF1 exhibits significant affinity for m^6A-containing probes, which is exclusively dependent on the presence of m^6A (**Supplemental Figure S4J**). Consistent with our RNA pulldown proteomics data, we also observed that m^6A modification repels TRA2B binding, resulting in a higher affinity for the unmethylated probe (**Supplemental Figure S4J**).

We also confirmed the interaction of FMRP with the unmethylated EPAP probe and observed enhanced affinity for the methylated probe (**Supplemental Figure S4J**). Furthermore, while FXR1P and FMRP bind the EPAP probe with comparable overall affinity, FXR1P exhibits a slightly pronounced preference for the m^6A-modified probe, in contrast to FMRP, which shows little discrimination between methylated and unmethylated sequences (**Supplemental Figure S4J**). The known heterodimerization of FXRs, combined with these findings, suggests that FXRs bind cooperatively to the m^6A-EPAP motif. We therefore used RNA-nHU to investigate whether the absence of FMRP affects FXR1P and FXR2P binding. In *Fmr1*-KO cortical neurons, the interaction between FXR1P and the m^6A-containing EPAP probe was decreased, suggesting that FXR1P, requires FMRP for a robust interaction with the EPAP motif (**Supplemental Figure S4J**).

FMRP has been described to influence the nuclear export and neurite transport of mRNAs (Dictenberg et al., 2008; Kao et al., 2010; Edens et al., 2019). To determine whether FMRP plays a similar role for *Dgkk* mRNA, we investigated its nuclear export and neurite transport. We isolated nuclei from the cytosol in both WT and *Fmr1*-KO brain samples to quantify mRNA level by qRT-PCR on each fraction. The enrichment of nuclear U2 snRNA in nuclei fraction confirmed the correct separation of nuclei and cytosol. However, we detected no difference in *Dgkk* mRNA levels between the nuclear and cytosolic fractions, indicating that FMRP does not influence the nuclear export of *Dgkk* mRNA (**Supplemental Figure S4K**).

Since m^6A regulates mRNA neurite transport (Loedige et al., 2023) and FMRP acts as an m^6A reader, we investigated whether the loss of FMRP alters *Dgkk* mRNA transport into neurites. To assess this, we cultured primary cortical neurons on filters to physically separate soma from neurites, subsequently quantifying mRNA levels by qRT-PCR in both fractions. The substantial enrichment of *Col3a1* mRNA, a previously established transported mRNA, and the more abundant level of *Gng3* mRNA in soma, known to be poorly transported, confirmed the proper quality of preparations (**Supplemental Figure S4L**). Our data showed that approximately 50% of *Dgkk* mRNA is transported into neurites, which is slightly exceeding the level observed for *Psd95* mRNA (~40%). Importantly, no transport defect was observed in *Fmr1*-KO neurons, indicating that *Dgkk* mRNA transport into neurites is independent of FMRP (**Supplemental Figure S4L**). These results suggest that FMRP is not involved in the regulation of *Dgkk* mRNA nuclear export or neurite transport. We therefore concluded that FMRP regulates DGKκ expression exclusively at the translational level.

Recent studies indicate that m^6A modifications within coding sequences, particularly on GAA codon (Glu), slow translation elongation and ultimately triggering ribosomal collisions (Mao et al., 2019; Linder et al., 2025; Murakami et al., 2025). Strikingly, the conserved m□A

consensus motif within the EPAP domain of DGKκ in both mouse and human corresponds to the GAACC context, with methylation occurring on the GAA codon. We investigated the function of m^6A in the N-terminal region of DGKκ, which contains the EPAP motif, using the nanoluciferase gene reporter system described above in non-neuronal cells. To assess the impact of m□A on the EPAP motif, cells were treated with *METTL3* siRNA. *METTL3* silencing resulted in a ~2.5-fold increase in N-ter-DGKκ-NLuc RNA levels, which was markedly higher than that observed for the control NLuc construct (**Supplemental Figure S4M**). Notably, this effect was specific to the EPAP motif, as its deletion in the ΔEPAP-NLuc construct, abolished this effect (**Supplemental Figure S4M**). These results are consistent with previous studies showing that m^6A modifications within the coding sequence promote efficient mRNA degradation (Zhou et al., 2024).

Surprisingly, however, luciferase activity from the N-ter-DGKκ-NLuc construct did not correlate with RNA abundance, leading to an ~80% reduction in translation efficiency (luciferase/RNA ratio) when silencing METTL3 compared with the control condition (**Fig. 4I**). This effect was also seen, in a dose-dependent manner using STM2457 METTL3 specific inhibitor (**Supplemental Figure S4N**). Interestingly, this effect that was not observed when the EPAP repeats or the proline-rich region were out of frame (**Fig. 4I**) and led to an increase or no change of translation efficiency in accordance with the literature. These results indicate that, within the context of exon 1 of DGKκ, m^6A modifications counteract a sequence-imposed translational repression, as FMRP, and positively regulate translation efficiency.

Moreover, this effect is independent of YTHDF1 and YTHDF2, as their silencing increased RNA level of N-ter-DGKκ-NLuc construct, without affecting its translation efficiency, consistent with their well-established roles in regulating mRNA stability (Murakami and Jaffrey, 2022) (**Supplemental Figure S4O**).

To determine whether the features of DGKκ binding site were shared with other mRNAs, we further analyzed our CLIP-seq data. Beyond the DGKκ, we detected 1,219 peaks overlapping at least an exon of a protein-coding gene on the same strand, for which we could retrieve the amino acid sequence. We analyzed the enrichment of FMRP peaks using a sliding codon-triplet window corresponding to 30 amino acids, approximately matching the peptide-length capacity of the ribosomal exit tunnel (**Supplemental Table S2**). Interestingly, FMRP-bound sequences are mostly enriched for proline relatively to the proteome (**Supplemental Figure S4P and supplemental Table S2**). Additionally, a subset of FMRP binding sites across the transcriptome localize to sequences encoding amino-acid repeats. Strikingly, the three most enriched amino acids triplets were RRS, PPP, and QQQ motifs known to negatively modulate elongation kinetics through interactions with the ribosomal exit tunnel (Zhao et al., 2021; Aguilar Rangel et al., 2024; Aviner et al., 2024) (**Fig. 4J**). Other enriched triplets predominantly encoded proline-rich, glutamine-rich, or charged amino-acid clusters, including the PEP and EPD tripeptides found in DGKκ (**Fig. 4J**). These findings are consistent with recent studies showing that FMRP preferentially associates with sequences where ribosomes pause on regions enriched in glutamate and aspartate, while not being directly involved in the establishment of the stalling (Anadolu et al., 2023; Li et al., 2025).

Interestingly, although all of these sequences can be associated with FMRP, only a small number of motifs, including the PEP and EPD motifs within the DGKκ EPAP repeat can contain a DRACH m□A consensus motif, suggesting that the m^6A-mediated effects of FMRP are highly restricted. This selective enrichment implies that FMRP may alleviate ribosome collisions at m□A-marked sites (e.g., PEP within the EPAP domain) to regulate the translation of neurodevelopmental effectors, while also modulating translation through m^6A-independent mechanisms, as observed for *Nisch* mRNA (**Supplemental Figure S4Q**). Within the EPAP domain, m□A may therefore represent an additional regulatory layer that promotes

the recruitment of FMRP and associated factors to fine-tune DGKκ translation. Conversely, we also identified m□A deposition on similar sequence contexts that do not exhibit detectable FMRP binding (**Supplemental Figure S4R**), indicating that m^6A alone is not sufficient for FMRP recruitment but may nevertheless regulate translation through related mechanisms. Collectively, we identify a previously unrecognized, heavily m□A-modified FMRP binding site on *Dgkk* mRNA, which we term "EPAP", encoding a tandemly repeated amino acid sequence. Our data uncover a novel function for both FMRP and m^6A in facilitating translation in the EPAP region intrinsically prone to ribosomal stalling due to its amino acid composition. More broadly, we show that a subset of FMRP binding events is associated with repetitive coding sequences linked to altered translation dynamics, suggesting that this mode of FMRP action extends beyond DGKκ to a wider class of transcripts.

Discussion

Here, we reveal the functional importance of the DGKκ enzyme in regulating neuronal DAG-signaling — a mechanism central to the adaptation to external stimuli in many cell types (Mérida et al., 2008; Almena and Merida, 2011; Eichmann and Lass, 2015; Cooke and Kazanietz, 2022)— and how FMRP contributes to its regulation. The balance of DAG and PA plays a pivotal role in intracellular signaling (Almena and Merida, 2011) and its dysregulation, as a consequence of DGKκ lack of expression, has been postulated as an underlying pathomechanism of FXS (Tabet et al., 2016a, 2016b). Despite a low and restricted expression in certain brain areas, the loss of DGKκ revealed both neuronal and non-neuronal phenotypes. At behavioral level, the *Dgkk*-KO model exhibits significant neurodevelopmental impairments, notably marked hyperactivity, reduced anxiety, hypersensitivity, and compulsive behavior, recurrent phenotypes of the *Fmr1*-KO mice (Kazdoba et al., 2014).

Consistently with other DGK mouse models (Kim et al., 2009; Shirai et al., 2010; Yang et al., 2011), these findings confirm the importance of DAG-associated lipid signaling in neurodevelopment.

Several physiological alterations have been reported in *Fmr1*-KO mice, including lipids and glucose metabolism defects associated with increased non-fat body mass including increased muscle mass and global skeleton length, evocative of an overgrowth phenotype (Leboucher et al., 2019b). These features are present in a proportion of FXS patients (Leboucher et al., 2019c; Ruggiero-Ruff et al., 2023). FMRP was proposed to impact the hormonal system and notably hypothalamic function, which could explain the non-neuronal phenotypes in FXS (Nowicki et al., 2007; Hardiman and Bratt, 2016; Muzar et al., 2016; Long et al., 2020; Ruggiero-Ruff et al., 2023). To date, the molecular origin of this phenotype is unknown. Interestingly, *Dgkk*-KO mice mirror, but even more prominently this overgrowth phenotype, likely due to the partial loss of DGKκ in *Fmr1*-KO mice (decrease by 50% in the hypothalamus). The high expression level of DGKκ in the hypothalamus and its lower level in *Fmr1*-KO mice raise further questions about the role of the hypothalamus in FXS and make DGKκ a relevant candidate to explain associated phenotypes.

Additionally, we detected cardiomyopathy in *Dgkk*-KO mice that is evocative of a condition commonly described in FXS patients but whose origin remains unexplored (Pyeritz et al., 1982; Hagerman and Synhorst, 1984; Loehr et al., 1986; Sreeram et al., 1989; Crabbe et al., 1993). Macroorchidism, however, a typical phenotype observed in FXS patients and the *Fmr1*-KO mouse model, is not exhibited by *Dgkk*-KO mice, suggesting that other FMRP mRNA targets participate in the plethora of FXS-associated phenotypes.

Dgkk-KO neurons exhibit exacerbated DAG-signaling pathways associated with a global increase of neuronal protein synthesis rate. Excessive neuronal translation is considered a hallmark of FXS condition and is proposed to underly LTP/LTD defects along with abnormal

dendritic spine morphology leading to synaptic defects and some behavioral alterations (Bear et al., 2004). The exact cause of this global translation increase in FXS was unclear and hypothesized to be a consequence of the loss of repression by FMRP acting individually on its multiple targets (Bear et al., 2004). Our data demonstrate that the excessive DAG-signaling consecutive to lack of DGKκ leads to such an effect and is the likely cause of global neuronal translation excess in FXS, affecting mostly those cells (like neurons) where DGKκ is expressed. The loss of DGKκ leads also to abnormal dendritic spine morphology and an impaired mGlurI-dependent neuronal activity. These data suggest that DGKκ loss by itself contributes to a large body of neuronal defects of FXS condition.

Overall, the *Dgkk*-KO mouse model recapitulates a substantial proportion of *Fmr1*-KO phenotypes, spanning behavioral, physiological, neuronal, and molecular levels. To our knowledge, no other validated FMRP mRNA target accounts to such an extent to the FXS-like phenotypes, highlighting the relevant and important contribution of DGKκ to the pathology.

The identification of the RNA binding properties of FMRP has been a long-standing question in the field of FXS research. While FMRP has been shown to interact with high affinity to specific RNA structures present in a limited number of mRNAs (e.g., G-quadruplexes, SoSLIP) (Bechara et al., 2009; Darnell et al., 2001; Schaeffer et al., 2001), it has also been shown to interact with short low-affinity RNA sequences present in nearly all mRNAs (e.g., ACUK, WGGA, CTGKA, U-rich) (Chen et al., 2003; Dolzhanskaya et al., 2003; Ascano et al., 2012; Maurin et al., 2018a), implying a dual recognition capability, possibly related to its several RNA binding domains, namely the KHs and the RGG domain.

The binding motif identified here is distinct from previously described motifs, yet similarly GC-rich and composed of a tandemly repeated GARCCGGCCCCA dodecamer. This motif

encodes a conserved and highly repeated EPAP amino acid sequences (~120 amino acids), consisting of approximately 80% acidic residues (aspartate and glutamate) and prolines, suggesting strong selective pressure to maintain this reading frame. Deletion of the N-terminal region of DGKκ increased its expression by approximately tenfold, while fusion of *Dgkk* exon 1 (containing the EPAP motif) upstream of a reporter gene strongly reduced reporter expression, revealing the presence of negative translational control elements. We show that this domain induces strong translational repression and ribosomal collisions specifically in the reading frame conserved through evolution, indicating that the effect is mediated by the encoded protein sequence rather than by RNA features. These data are consistent with recent studies indicating that ribosomes are globally prone to stalling on sequences encoding clusters of glutamate, aspartate, and proline residues (Chyżyńska et al., 2021; Aguilar Rangel et al., 2024; Ichihara et al., 2025; Uematsu and Qian, 2025). Moreover, disome-seq analyses have revealed that ribosomal collisions occur preferentially at clusters of charged amino acids, including both negatively charged (aspartate, glutamate) and positively charged (arginine, lysine) residues (Arpat et al., 2020; Han et al., 2020; Zhao et al., 2021). Importantly, fusion of the EPAP motif to a luciferase reporter was sufficient to recapitulate FMRP-dependent translational control in neurons. This control depends on the reading frame that induces ribosomal stalling in the EPAP motif, suggesting that, FMRP alleviates translation repression imposed by the sequence. Interestingly, the EPAP motifs perfectly overlap with a unique and strong m^6A peak in *Dgkk* mRNA. Due to its distinctive location in *Dgkk* exon 1, we hypothesize that EPAP m^6A function may diverge from m^6A sites typically observed around stop codons, described to modulate mRNA decay (Murakami and Jaffrey, 2022). Mass-spectrometry-based interaction screening had identified FMRP as potential m^6A reader playing a role in translation control (Edupuganti et al., 2017), and polyribosome-associated FMRP mRNA targets showed high levels of m^6A modification suggesting that m^6A marks

could be used for selective recognition (Chang et al., 2017). FMRP can bind m^6A consensus sequences in vitro, although rather inefficiently and with some selectivity depending of the consensus sequence (Edens et al., 2019; Hsu et al., 2019; Worpenberg et al., 2021b; Zhang et al., 2022a).

The EPAP motif contains multiple of the less frequent GAACC m^6A consensus site and its methylation status seems to determine FMRP binding efficiency since decreasing m^6A level greatly impaired DGKκ mRNA binding in neurons and in vitro. Our results confirm the selectivity of FMRP for specific m^6A consensus sites and suggest that its exceptionally high affinity for *Dgkk* mRNA is due to the unique repetitive nature of its binding site combined with the high density of m^6A modifications within that region.

Recent studies have shown that m^6A within coding sequences can negatively modulate elongation kinetics (Choi et al., 2016; Linder et al., 2025; Murakami et al., 2025) particularly when occurring on GAA codons. Interestingly, the conserved DRACH motif within the EPAP sequences (GAACC) between mouse and human restricts methylation specifically to the GAA context. Strikingly, our data indicate that when depleting m^6A in the EPAP motif context, translation efficiency is dramatically decreased. These data indicate that m^6A, in this context, contribute positively to translation, in contrast with previously known function of m^6A. Moreover, this translation control is, as for FMRP, specific to the context inducing strong translational repression.

FMRP has been proposed to sequester YTHDF1 and to release it upon phosphorylation to promote translation of the YTHDF1 mRNA targets (Zou et al., 2023). Additionally, work in drosophila have suggested that recruitment of dFMRP to m^6A RNAs is via its interaction with dYTHDF (Worpenberg et al., 2021). The DGKκ control clearly diverge from these mechanisms. Indeed, YTHDF proteins are also recruited to the EPAP motif; however, our data do not support a role for YTHDFs in regulating DGKκ translation. Our findings

demonstrate that FMRP promotes DGKκ mRNA translation, highlighting a nuanced role that extends beyond its canonical function as a translational repressor. This observation aligns with studies showing that FMRP can positively regulate translation of large autism-related protein (Greenblatt and Spradling, 2018). Similarly, studies in mouse have reported that FMRP preferentially associates with sequences that induce ribosomal stalling—particularly aspartate- and glutamate-rich regions—without being directly responsible for the stalling itself (Anadolu et al., 2023; Li et al., 2025). Consistent with this, analysis of our CLIP data reveals that a subset of FMRP binding events occurs on repetitive sequences enriched in proline, as well as other amino acid repeats known to alter translation dynamics, including clusters of positively and negatively charged residues (Aguilar Rangel et al., 2024) and polyglutamine stretches (Aviner et al., 2024). Most of these motifs are encoded by GC rich codon which potentially create secondary structure that might be involved in FMRP recruitment (e.g. G-quadruplex). Of note, only a fraction of these motifs contains a DRACH consensus and bears m^6A modifications, including the abundant PEP motif within the DGKκ EPAP domain. These observations indicate that m^6A is not strictly required for FMRP binding and that FMRP can function in an m□A-independent manner. We propose that m^6A instead constitutes an additional regulatory layer that can enhance FMRP recruitment and, independently, modulate translation on stall-prone sequences.

More broadly, the convergence of FMRP binding and m^6A deposition—both traditionally associated with translational repression—on sequences that intrinsically induce ribosomal stalling raises important mechanistic questions. Together, our findings support a model in which FMRP exerts a context-dependent dual function in translational control: beyond its well-established repressive role, on intrinsically stall-prone coding sequences FMRP-mediated attenuation of ribosome kinetics may instead be beneficial, locally mitigating ribosomal collisions and ultimately enhancing productive translation (**Fig. 4K**). In this

framework, FMRP emerges not simply as a brake on protein synthesis, but as a regulator of translational flow, fine-tuning ribosome behavior to modulate the expression of neurodevelopmental effectors in response to the intrinsic properties of the coding sequence.

Material and methods

Animal model

Dgkk$^{em1(IMPC)Ics}$ (*Dgkk*-KO) in C57BL/6NCrl background was obtained through Infrafrontier-I3 program by CRISPR/Cas9 deletion of exon 8 (GRCm38.p4 6897240/6897601, details available on www.mousephenotype.org. Males from the same genotype (thereafter called *Dgkk*-KO or *Dgkk*-WT) were grouped by 3 or 4 individuals at weaning age (4 weeks), in individually ventilated cages (GM500, Tecniplast, UK), with poplar shaving bedding (Lignocell Select, JRS, Germany), and maintained under standard conditions on a 12-h light/dark cycle (7 h/19 h) with standard diet food (standard diet D04, Scientific Animal Food and Engineering, France) and water available ad libitum. Mice from the same cage received the same treatment and were transferred in the phenotyping area the next week. Animal work involved in this study was conducted according to ARRIVE guidelines and received authorization from relevant national committee (Comité National de Reflexion Ethique en Experimentation Animale) with APAFIS #17544-2018111516571205 v7 at the ICS mouse facility (Illkirch, France). Every procedure on mice was performed to ensure that discomfort, distress, pain, and injury would be minimal.

Genotyping

Genotyping was performed after birth on tail genomic DNA by PCR using primers CCTTCAGCAGCCTACCAACATTG and CTTCCGAAGGAACATTCCTTGG producing a 334 amplicon in WT and no product in KO, primers CCAAGGAATGTTCCTTCGGAAG and GAACATGCCCATACTCATGTACCC producing a 288 bp amplicon in WT and no product in KO, and primers CCTTCAGCAGCCTACCAACATTG and GAACATGCCCATACTCATGTACCC producing a 241 bp amplicon in KO and no product in WT.

Behavioral experiments

Behavioral experiments were conducted at 10 weeks. The behavioral experiments were performed under experimenter-independent conditions or by experimenters naive to the treatment conditions. Individual cohorts of male littermate animals (issued from *Dgkk*$^{y/+}$ x *Dgkk*$^{+/-}$ mating) were composed of WT and *Dgkk*-KO subgroups.

Elevated plus maze

The apparatus used is automated and made of PVC (Imetronic, Pessac, France). Two open arms (30 Å~ 5 cm) opposite one to the other and crossed by two closed arms (30 Å~ 5 Å~ 15 cm). The maze has infrared captors allowing the detection of mice in the closed arms and different areas of the open arms. The mice were tested during 5 min. The number of entries and time spent in the open arms were measured to calculate an index of anxiety.

Nest building

On the day of test, mice were singly transferred in a standard cage for the duration of nest building measurement. A block of nesting material (5 Å~ 5 cm hemp square, Happi Mats, Utopia) was placed in the cage. Pictures were taken and visual scoring occurred at 2, 5, 24 h without disturbing the animals. The room temperature was noted when the nest was scored since nest building has a thermoregulatory function and therefore may be influenced by ambient temperatures. We used a 0-5 scale described by (Gaskill et al., 2013): 0 = undisturbed nesting material; 1 = disturbed nesting material but no nest site; 2 = a flat nest without walls; 3 = a cup nest with a wall less than the height of a dome that would cover a mouse; 4 = an incomplete dome with a wall of the height of a dome; 5 = a complete dome with walls taller than the height of a dome, which may or may not fully enclose the nest.

Marble burying

Twenty glass marbles were placed equidistant from each other on the litter of the cages. The mice were left in contact with the marbles for a total period of 30-min. The test was terminated by removing the mice from the cages. The number of marbles was counted after 30 min. A marble was considered buried when two-thirds or more of it was covered with burying substrate.

Novel object recognition task

Mice were tested in a circular arena (50 cm diameter and 30 cm height basin). The locomotor activity was recorded with the EthoVision XT video tracking system (Noldus, Wageningen,

Netherlands). The arena was homogeneously illuminated (40 Lux) divided into central and peripheral regions. First, animals were habituated to the arena for 15 min. Each mouse was placed in the periphery of the arena and allowed to explore the apparatus. Experimenter were out of the sight of the tested animal. During the test session, the distance traveled and time spent in the central and peripheral regions were recorded. The percentage of time spent in center area was used as index of anxiety. The following day, mice were tested for object recognition in the same arena. Mice were tested for a 10-min acquisition during which they were placed in the arena in presence of a sample objects (2.5 cm diameter marble or 2 cm edge plastic dice). The time took by the animal to explore the samples was manually recorded. The following day, a 10-min retention trial was conducted. During this retention trial, the samples A and another object B (marble or dice depending on acquisition) were placed in the open field. The times took to explore the object A and object B by the animal were recorded. A recognition index was calculated as (tB / [tA + tB]) x100.

Social recognition test

Social recognition test evaluates the preference of a mouse for a congener as compared to an object placed in an opposite compartment. This test is also used for evaluation of social memory by measuring exploration of a novel congener as compared to a familiar one. The apparatus is a transparent cage composed with a central starting compartment and two side compartments where circular grid cup (goal box) is placed at each extremity, and where the congener can be placed during testing. Testing was performed for 2 consecutive days. On the first day, the mouse was placed in central box then allowed to explore freely the apparatus for 10 min to attenuate their emotionality. On the second day, a C57BL/6NCrl congener from the same sex was placed in one goal box and an object was placed in the opposite one. The mouse was then placed in the starting central compartment and allowed to explore freely the apparatus for 10 min. The position of the congener and object boxes was counterbalanced to avoid any potential spatial preference. The duration of exploration of each goal box (when the mouse is sniffing the grid delimiting the goal box) was manually measured and the percentage of time the mouse took to explore the congener was used as index of social preference (recognition preference). A 10-min retention trial was then performed during which the object was replaced by a novel congener. The duration of exploration of each goal box was manually measured and the percentage of time the mouse takes to explore the congener was used as index of social memory. The social preference index (SR) is defined as (time Congener /

[time Object + time Congener])x100; and the social memory index as (time novel Congener / [familiar congener + time novel Congener])x100.

PRM-based quantification of DGKκ in tissues

Skyline software was used for the *in-silico* identification of signature peptides based on the following criteria: peptide length of 7 to 25 amino acids, excluding the first 25 N-terminal residues that could potentially constitute a signal peptide; peptides must be unique to the protein of interest (proteotypic); avoid peptides containing Cys (tends to form disulfide bonds), Met (prone to oxidation), Arg-Pro/Lys-Pro (promote missed cleavages), Asn-X-Thr/Asn-X-Ser (sites of N-glycosylation). It is important to select target peptides that are not affected by uncontrolled modifications since these lead to changes in the molecular weight of the peptide, which would appear in two forms and could no longer be considered a signature peptide. A list of mouse DGKκ peptides that meet these requirements was generated and spectral matches were found in the predictive library Prosit. Prosit was built using a deep learning algorithm that was trained with mass spectra obtained from MS analysis of synthetic reference peptides (Gessulat et al., 2019). However, experimental spectra for the signature DGKκ peptides were not found in proteomics databases (NIST, GPM, PeptideAtlas), so they needed to be validated empirically. We designed and identified on Skyline software two theoretical DGKκ -specific peptides (P06 and P07). This strategy required validation of the selected peptides and prior information such as elution time, m/z value, charge state, and fragmentation conditions, which is obtained during preliminary measurements by a global acquisition method (DDA) of the target protein produced in an overexpression system (Zhang et al., 2022b). The target peptides are then synthesized chemically with heavy isotopes that incorporate 13C- and 15N-labeled C-terminal arginine (R) or lysine (K), identical in sequence and physicochemical properties to the peptides of interest, that are needed for the actual spiking and quantification of the samples. To improve the precision of absolute abundance measurements, an external calibration curve is produced by measuring the signal intensity of the reference peptides at multiple concentration points. Spike-in of samples with heavy-labeled peptides is used as internal standards.

Frozen cell pellets or tissues were lysed in RIPA lysis buffer [50 mM Tris-HCl pH 7.4, 0.08 mM CaCl2, 100 mM KCl, 1 mM MgCl2, 1% (v/v) NP-40, 0.5% (m/v) sodium deoxycholate, 1% (m/v) SDS, 1× cOmplete EDTA-free protease inhibitor cocktail] and protein concentration was determined using Bradford method (Bio-Rad protein assay dye reagent,

#5000006). A total of 20 μg of protein extracts were migrated for 15 minutes at 150 V on a 10 % SDS-PAGE gel. Subsequently, the gel was fixed for 30 minutes in a solution containing 10% (v/v) acetic acid and 40% (v/v) ethanol, followed by staining with PageBlue Protein Staining Solution (ThermoScientific) for 1 hour. After multiple washes with ultrapure water, a band corresponding to the expected molecular weight of DGKκ was excised. Gel strips were transferred to a 96-well microplate and de-stained by washing three times with 50 mM ammonium bicarbonate (Sigma) and 50% (v/v) acetonitrile (Biosolve) for 10 minutes at room temperature with agitation at 850 rpm, followed by a wash with 100% acetonitrile under the same conditions. The gel bands were then reduced with 10 mM DTT for 30 minutes at 56°C, followed by alkylation with 50 mM IAA for 30 minutes in the dark. Gel strips were washed again using the same procedure and dried in a SpeedVac for 15 minutes.

Digestion was performed overnight at 37°C using trypsin at a concentration of 10 ng/μl diluted in 10% (v/v) acetonitrile, 50 mM ammonium bicarbonate, and 2 mM CaCl2. Peptides were extracted first with 0.2% (v/v) formic acid and 50% (v/v) acetonitrile for 15 minutes at room temperature with agitation at 850 rpm, followed by extraction with 0.2% (v/v) formic acid and 90% (v/v) acetonitrile using the same conditions, pooling two gel bands per condition. Finally, the peptide mixture was dried in a SpeedVac for approximately 3 hours, resuspended in 20 μl of 0.1% (v/v) trifluoroacetic acid (TFA), and 0.5 μl was injected into the mass spectrometer.

Neuronal primary culture

Cortices, hippocampi, or hypothalami from C57BL/6J WT or *Fmr1*-KO E17.5 mouse embryos were dissected in dissection buffer containing 1xPBS, 2.56 mg/mL D-glucose, 3 mg/mL BSA, and 1.16 mM MgSO4. Each brain tissue was then incubated for 25 minutes in 100 μL of dissociation buffer composed of Neurobasal medium (GIBCO), 20 U/mL papain (Worthington), and 1 mg/mL DNase I. After centrifugation at 1000 × g for 5 minutes, the dissociation solution was discarded, and 500 μL of ovomucoid (Worthington) inhibitory solution was added and incubated for 6-7 minutes. Following this incubation, the ovomucoid solution was removed, and the cells were gently mechanically dissociated by pipetting 15 times to achieve a single-cell suspension. The dissociated cells were plated on poly-L-lysine hydrobromide-coated (P9155, Sigma) culture plates and cultured for 8 to 21 days in Neurobasal Medium supplemented with B27, penicillin/streptomycin, and 0.5 μM L-glutamine. Half of the media were changed every 2-3 days. For experiments requiring

puromycin treatment, cultures were treated with puromycin solution at specified concentrations and durations as indicated.

Western-blot

The cell lysates in the Laemmli buffer blue were heated for 5 minutes at 95°C, and 8 µL (equivalent to 15 µg of total protein) were loaded onto an SDS-PAGE denaturing gel composed of a stacking gel [4% (w/v) acrylamide/bisacrylamide 29:1 (v/v); 0.1 M Tris-HCl pH 6.8; 0.1% (w/v) SDS; 0.1% (w/v) APS; 0.01% (w/v) TEMED] and a resolving gel [10% (w/v) acrylamide/bisacrylamide 29:1 (v/v); 0.375 M Tris-HCl pH 8.8; 0.1% (w/v) SDS; 0.1% (w/v) APS; 0.01% (w/v) TEMED]. A molecular weight marker (PageRuler™ Plus Prestained Protein Ladder) was also loaded. The gel was run at 150 V for 1 hour in Tris/Glycine/SDS running buffer [0.001 M Tris-HCl; 0.2 M Glycine; 0.1% (w/v) SDS]. The transfer was performed onto a PVDF membrane (0.22 µM, Millipore) activated for 5 minutes in 100% ethanol, for 1.5 hours at 200 mA in Tris/Glycine/SDS/Ethanol transfer buffer [0.001 M Tris-HCl; 0.2 M Glycine; 0.1% (w/v) SDS; 20% (v/v) ethanol]. The PVDF membrane was then blocked with a solution of TBS (50 mM Tris-HCl pH 7.6; 150 mM NaCl) and 0.1% (v/v) Tween-20 with 5% (w/v) skim milk powder. The primary antibody diluted in TBS-0.1% (v/v) Tween-20 solution with 5% (m/v) of skim milk powder was incubated with the membrane at 4°C for 12 hours. After 3 washes of 15 minutes with gentle agitation in TBS-0.1% (v/v) Tween-20 solution, the membrane was incubated with HRP-conjugated secondary antibody (horseradish peroxidase – goat anti-mouse or rabbit J. Immunoresearch SA, 1:10000) in the same solution at room temperature for 1 hour. After 3 more washes of 15 minutes as previously described, the proteins of interest were detected using Immobilon reagent (Millipore) and visualized with a LAS600 imager (Amersham).

qRT-PCR

Total RNA was prepared from neurons or tissue using 700 µL of TRIZOL reagent (Invitrogen) according to the manufacturer's instructions. The RNA was then precipitated for 12 hours with two volumes of 100% isopropanol at -20°C. After centrifugation for 10 minutes at 13,000 rpm at 4°C, the supernatant was removed, and the RNA pellet was washed three times with 70% ethanol (v/v). The pellet was then resuspended in 10 µL of mQ water, and the RNA concentration was measured using a Nanodrop device. A DNase Turbo (ThermoFisher, 65001) treatment was performed on 4 µg of RNA for 30 minutes at 37°C with 1 U of the enzyme to eliminate any contamination by genomic DNA.

Reverse transcription was performed with SuperScript IV reverse transcriptase (Invitrogen) using 500 ng of purified total RNA according to the manufacturer's instructions. qPCR was performed with the LightCycler 480 SYBR Green I Master (Roche) according to the manufacturer's instructions using the Roche LightCycler 480 device with an activation cycle of 15 minutes at 95°C and 45 amplification cycles (15 seconds at 95°C, 30 seconds at 60°C, 30 seconds at 70°C).

Immunofluorescence

Cells on coverslips were washed twice with 1x PBS to remove any residual media or debris. Subsequently, they were fixed with 4% (v/v) formaldehyde and 4% (m/v) sucrose in 1x PBS for 20 minutes. After fixation, the samples were washed twice again with 1x PBS. Permeabilization was carried out using 0.2% (v/v) Triton X-100 in 1x PBS for 10 minutes. For the blocking of aspecific sites, samples were incubated in a blocking buffer containing 1x PBS, 3% (m/v) bovine serum albumin (BSA), and 0.02% (v/v) Triton X-100 for 1 hour. Primary antibody incubation was performed overnight at 4°C. The primary antibody was diluted in a buffer containing 0.02% (v/v) Triton X-100 and 0.2% BSA (m/v). The next day, samples were washed three times for 10 minutes each with PBS containing 0.02% (v/v) Triton X-100 and 0.2% (m/v) BSA. Coverslips were then incubated for 1-2 hours at room temperature with fluorophore-conjugated secondary antibodies, diluted 1:1000 in the same buffer used for the primary antibody. After the secondary antibody incubation, samples were washed again three times for 10 minutes each with PBS containing 0.02% (v/v) Triton X-100 and 0.2% (m/v) BSA. Finally, the samples were mounted with Fluoromount and sealed with nail polish to prevent drying and preserve fluorescence.

Dendritic spine morphology classification

Hippocampal primary neurons were magnetofected using NeuroMag (OzBiosciences) with a GFP plasmid at 3DIV. At 21DIV, neurons were immunolabeled using a GFP-specific antibody to enhance the signal. Selected isolated dendrites were imaged using confocal microscopy (Leica SP8X) with a 63X objective and a resolution of 4096x4096 pixels, with a step size of 0.2 µm to generate a stack of images for subsequent automated analysis using Imaris software. The following parameters were used to automatically classify dendritic spine according to their morphology: stubby: spine length < 1 µm; mushroom: spine length < 3 µm and max head width > mean neck width x 1.5; long thin: mean head width ≥ mean neck width and spine length > 1.5 µm; filopodia: spine length > 2 µm.

MEA recording

High-density MEA Accura (3Brain) chips having 4096 electrodes were sterilized by filling the reservoir with 70% (v/v) ethanol for 20 minutes. Subsequently, the chips were rinsed three times with sterile mQ water. Once dried, the central areas of the chip, which contain the electrodes, were double-coated overnight with poly-D-lysine (P9155, Sigma) and bovine fibronectin (F1141, Sigma). Following three additional washes with mQ water, exactly 80,000 dissociated primary neuronal progenitors were seeded onto the dry chips. After allowing 1 hour for cell attachment, the reservoir was filled with Neurobasal Medium supplemented with B27. Throughout the experiment, the chips were maintained at 37°C with 5% CO2 in a 10 cm Petri dish with a smaller dish containing water to prevent media evaporation. Neurons were fed every 2 days by replacing half of the media with pre-heated media. At 21DIV, the HD-MEA chips were connected to the Biocam X device for recording neuronal activity using BrainWave 5 software. For DHPG treatment, a solution of 200 µM DHPG diluted in Neurobasal Medium supplemented with B27 was prepared and pre-heated at 37°C. For neuronal activation, while recording, half of the media in the HD-MEA chip was replaced with the DHPG-containing Neurobasal Medium supplemented with B27 to achieve a final concentration of 100 µM DHPG.

CLIP

CLIP analysis was performed as described in (Tabet et al. 2016a). Briefly, Neuronal cultures at 8DIV were rinsed once with cold 1x PBS, and then proceeded for UV crosslinking (254 nm, 400 J/cm^2, Stratalinker) on ice. Neurons from 2 wells of 6-well plate equivalent to one embryo were lysed in 400 µL of lysis buffer [50 mM Tris·HCl, pH 7.4, 100 mM KCl, 1 mM MgCl2, 0.1 mM CaCl2, 0.1% SDS, 1% Nonidet P-40, 0.5% sodium deoxycholate, 30 U of RNasin (Promega), and 10 U of DNase Turbo (Invitrogen)] and incubated for 5 min at 37 °C. Lysates were spun down at 18,000 g at 4 °C, and supernatants were precleared by incubation with 25 µL of free Dynabeads protein G (ThermoFisher) and then on 25 µL of Dynabeads protein G coupled to rabbit anti-mouse IgGs (2.5 µg) for 1 h each. The lysates were then incubated overnight with agitation on 25 µL of Dynabeads protein G coupled to 2.5 µg of anti-FMRP antibody (ab264380, Abcam). Importantly, although RNase treatment of immunoprecipitated RNA was not performed, partial RNA digestion occurs during the overnight incubation. After immunoprecipitation, the supernatants were saved for RNA extraction (WT and *Fmr1*-KO “inputs”), and the beads were washed three times with 400 µL

of high-salt washing buffer [50 mM Tris·HCl, pH 7.4, 1 M KCl, 1 mM EDTA, 1% (v/v) Nonidet P-40, 0.5% (m/v) sodium deoxycholate, and 0.1% (v/v) SDS; 4 °C]. RNAs from WT and *Fmr1*-KO neurons were recovered by treatment of the beads with 0.4 mg of proteinase K in buffer (100 mM Tris·HCl, pH 7.4, 50 mM NaCl, and 10 mM EDTA) for 20 min at 37 °C. The anti-FMRP antibody was selected among several tested antibodies based on its ability to immunoprecipitated efficiently some mRNAs considered as validated FMRP targets (i.e., *Dlg4*, *Map1b*) compared with mRNAs considered as non-FMRP targets (*Rplp0*) in WT compared with *Fmr1*-KO neuron extracts as quantified by qRT-PCR.

RNA isolation and sequencing

RNA was extracted from WT or *Fmr1*-KO neuron inputs (Input WT) or from CLIP samples (CLIP WT and CLIP *Fmr1*-KO) using phenol/chloroform (vol/vol) followed by chloroform/isoamyl alcohol (24:1) extraction and ethanol precipitation in the presence of 0.3 M sodium acetate. Subsequently, total RNA was treated with DNase (Invitrogen, AM1907) and 500 ng of RNA was ribodepleted using the Mouse-Rat RiboPOOL kit (siTOOLs Biotech, catalog no. dp-K012-055) according to the manufacturer's protocol, followed by reverse transcription using SuperScript IV (ThermoFisher, 18090200). For the HITS-CLIP strategy in hypothalamic neurons, reverse transcription was conducted with random hexamers following the manufacturer's protocol (ThermoFisher, N8080127). For the iCLIP strategy in cortical neurons, a set of 18 *Dgkk*-specific primers was utilized to cover the entire transcript of *Dgkk* and optimize RNA-seq coverage.

To enhance primer hybridization to *Dgkk* mRNA, we modified the reverse transcription protocol: after 5 minutes of RNA denaturation at 65°C, a hot start at 55°C was initiated by adding the reverse transcriptase mix directly to the RNA. Unlike random hexamers, which can initiate reverse transcription at multiple sites, this method allows reverse transcriptase to start only at the specific positions defined by the primers. This approach helps in blocking reinitiation when encountering FMRP polypeptide generated by proteinase K digestion, resulting in an enrichment of transcript stop at the same 5' location. Generated cDNA was treated with 1 µL of RNase A (5 µg/mL) for 20 minutes at 37°C, then purified using RNA XP beads (Beckman Coulter) at a 1.8x ratio. The purified cDNA was sonicated in Covaris microtubes (AFA fiber Snap-cap). Finally, the fragmented cDNA was repurified with RNA XP beads and processed for MeDIP library preparation.

EMSA

The FMRP full-length protein (Isoform 1) was prepared as a fusion protein with GST in a baculovirus system according to Bardoni et al. (1999). His–FMRP was eluted from NiNTA beads (Qiagen) in elution buffer (50 mM Tris–HCl pH 7.5, 1 mM MgCl2, 150 mM KCl, 1 mM EDTA, 1 mM DTT, 0.5M urea, 500 mM Imidazole). For binding assays, RNAs (5'GCCGGCCCCAGAGCCGG(m^6A)CCCCGA(m^6A)CCAG(m^6A)CUCAGAGCCGGCCCCAGAGCCGG(m^6A)CCCCGA(m^6A)CCAG(m^6A)CUCAGA(m^6A)CCG-Biotin 3') 5′-end labeling of RNA was performed with T4 polynucleotide kinase and [γ-32P] ATP. Labeled RNAs were purified on an 8% polyacrylamide gel (Acryl/Bisacrylamide 19/1, EU0061-B, Euromodex) in 8 M urea. Gel retardation assay. Labeled RNAs (40 000 c.p.m.), renatured for 10 min at 40°C in binding buffer (10 mM HEPES, pH 7.4, 50 mM KCl, 1 mM DDT, 1 mM EDTA, 0.05% TritonX-100, 5% (v/v) glycerol, 1µg/µl yeast tRNA, and 2 U/µl ribonuclease inhibitor) were incubated in 10 µl of binding buffer with 0–0.5 pmol at 25°C for 30 min. The mixture was loaded on a 4% polyacrylamide gel (bisacrylamide:acrylamide 1:37.5, 2.5% (v/v) glycerol, 0.5× TBE) and migration was performed for 1h at 300 V at 4°C. The gel was then subjected to phosphoimaging.

RNA- nHU

Protein-nHU analysis adapted from Zambo et al., 2022 (Zambo et al., 2022b), was applied to RNA as follows: At 8 days *in vitro* (8DIV), cortical neuronal cultures equivalent to those from three embryos were washed once with cold 1x PBS, pelleted at 1000g for 5 min at 4°C, and snap-frozen in liquid nitrogen. The pellets were lysed in ice-cold lysis buffer (50 mM Hepes-KOH pH 7.5, 100 mM NaCl, 50 mM KCl, 4 mM MgCl2, 1% (v/v) TritonX, 0.5 mM DTT, 1× cOmplete EDTA-free protease inhibitor cocktail, 5 mM TCEP, 10% (v/v) glycerol, and 500 U/mL of RNasin). Lysates underwent four rounds of sonication (4 × 20 s with 1-s pulses) on ice and were then incubated rotating at 4°C for 30 min. After centrifugation at 12,000 rpm at 4°C for 20 min, the supernatant was collected for further analysis. Total protein concentration was determined using the Bradford method (Bio-Rad protein assay dye reagent, no. 5000006) with a BSA calibration curve (MP Biomedicals, no. 160069), measured on a Bio-Rad SmartSpec 3000 spectrophotometer. Lysates were diluted to a concentration of 1 mg/ml.

For saturating streptavidin resin with biotinylated RNA probes or biotin, 50 µl of streptavidin resin was mixed with biotin or RNA probes at 20 µM concentration in 6 to 6.5 volumes of resin for 60 min. Specifically, streptavidin resin (Streptavidin Sepharose High Performance, Cytiva) was saturated with biotinylated EPAP RNA probes, with or without m^6A

modifications, at a concentration of 20 µM in 20 volumes of resin for 60 min. After saturation, the resins were washed once with 10 volumes of holdup buffer (50 mM Tris-HCL pH 7.5, 300 mM NaCl, 1 mM TCEP, 40 U/mL RNasin, 0.22-µm filtered), and any remaining streptavidin beads were blocked with 100 µM biotin in 10 volumes of holdup buffer for 10 min. Finally, the resins were washed twice with 10 volumes of holdup buffer. The nHU mixture was then incubated at 4°C for 1 hour. After incubation, the resin was separated from the supernatant by brief centrifugation (15 s, 2000 g), and half of the supernatant was immediately pipetted off to prevent resin contamination.

RNA pull-down

For beads coupling, 45 µL of Dynabeads MyOne Streptavidin (ThermoFischer, 65001) were incubated with RNA binding buffer (50 mM HEPES, pH 7.5, 150 mM NaCl, 0.5% (v/v) NP40, 10 mM MgCl2) containing 0.8 U/µL RNasin (Promega) for 30 minutes on ice. After removing the supernatant to eliminate RNAse-RNasin complexes, the beads were blocked in RNA binding buffer supplemented with 50 µg/mL yeast tRNA for 1 hour at 4°C under head-over-tail agitation. Following two washes with RNA binding buffer, 5 µg of RNA probes were added to the beads in 600 µL of RNA binding buffer and incubated for 1 hour at 4°C under head-over-tail agitation. Subsequently, RNA-bead complexes were washed twice with RNA binding buffer and twice with lysis buffer (50 mM Tris-HCl, pH 7.5, 150 mM KCl, 1 mM MgCl2, 1 mM EDTA, 1% (v/v) NP40, 0.5 mM DTT, 1× cOmplete EDTA-free protease inhibitor cocktail, 2.5% (v/v) glycerol, RNasin 200 U/mL).

Pellets of cortical neurons, equivalent to 5 embryos, were lysed in 300 µL of lysis buffer and incubated for 15 minutes at 4°C under head-over-tail agitation. After centrifugation at 1000 x g for 10 minutes at 4°C, the pellets corresponding to the nuclei fraction were resuspended in 300 µL of lysis buffer, sonicated (5 x 30 seconds pulses), and combined with the cytosol fraction. Lysates were then centrifuged at 18,000 x g for 10 minutes at 4°C, and protein concentration was determined using the Bradford method. Subsequently, 500 µg of protein lysate was incubated with RNA-bead complexes in 600 µL of lysis buffer for 1 hour under head-over-tail agitation. Finally, beads were washed three times with lysis buffer and stored dried at -20°C until proteomic analysis.

Northern-blot

Cell pellets were lysed on ice in 300 µL lysis buffer consisting of 50 mM Tris-HCl pH 7,5, 5 mM MgCl2, 150 mM KCl, 1 mM DTT, 0.5% NP-40, cycloheximide (100 µg/mL final), and

protease inhibitor cocktail. After gentle pipetting, lysate was centrifuged at 7000 x g for 8 min and RNA concentration was quantified using the Qubit BR RNA assay (Thermo Fisher).
An aliquot corresponding to 25 µg total RNA was adjusted to 300 µL using lysis buffer, and RNase A digestion was initiated by addition of 0.8 µg RNase A (Thermo Fisher, R1253). Samples were incubated at 25 °C for 20 min. Digestions were stopped by addition of TRIzol (Invitrogen) and RNA was extracted according to the manufacturer's instructions. Ten micrograms of purified RNA were loaded per lane for subsequent Northern blot analysis. After migration, gel was stained with ethidium bromide for imaging and RNA was electrotransfered onto a positively charged nylon membrane (Cytivia, 25006218) and proceeded twice to UV crosslinking (254 nm, 1200 J, Stratalinker).

PCR product (~ 400 nt) spanning the region of interest were radioactively labeled using random priming. Briefly, 100 ng of purified DNA probe were mixed with 2 µL of random hexamers (Thermo Fisher, N8080127) in a final volume of 15 µL, heated to 95 °C for 5 min, and rapidly chilled on ice for ≥2 min. The denatured probes were then combined with 6 µL of cold dNTP mix (0.5 mM each of dATP, dGTP, and dTTP), 5 µL of 10x Klenow buffer, 5 µL of [α-32P]-dCTP, 1 µL of Klenow fragment (Thermo Fisher), and nuclease-free water to a final reaction volume of 50 µL. The labeling reaction was incubated at 37 °C for 2 h. Probes were then purified using MicroSpin G-50 columns (Cytivia, 27533001).
Following labeling, probes were diluted by adding 760 µL of nuclease-free water. For hybridization, 400 µL of probe (~50 ng DNA) were heated to 95 °C for 5 min to denature, then immediately added to ~5 mL of hybridization solution (6x SSC [150 mM NaCl, 15 mM sodium citrate], 0.5% SDS). Membranes were incubated with the denatured probe overnight at 60 °C. Membranes were washed twice with SSC 2x, and once with SSC 2x, 0.1 % SDS for 10 min at 60°C. Finally, the membranes were then subjected to phosphoimaging.

Peak calling, fitration and annotation

The analyses of the CLIP-Seq dataset were implemented on Galaxy (Afgan et al., 2018)a. The protocol was adapted from (Heyl et al., 2026). In brief, adapters were removed and reads from fastq files of CLIP-Seq (IP) and bluk RNA-Seq (Input) were trimmed using Trimmomatic (Bolger et al., 2014) (Galaxy Version 0.39+galaxy2). Reads were then aligned on the Mouse reference genome mm39 using STAR (Dobin et al., 2013) (Galaxy Version 2.7.11b+galaxy0). Duplicates were removed with Sambamba (Tarasov et al., 2015) (Galaxy Version 1.0.1+galaxy2). Peaks were called using PEAKachu (https://github.com/tbischler/PEAKachu)

(Galaxy Version 0.2.0+galaxy0), with the bam of bulk RNA-Seq data as control. Simultaneously, we estimated gene expression by counting reads aligned on each gene as define in the reference annotation Gencode v. M38 with FeatureCounts (Liao et al., 2014) (Galaxy Version 2.1.1+galaxy0). Only genes with a count of at least 50 reads in either CLIP-Seq data or RNA-Seq data were further analyzed. We performed a differential expression analysis between RNA-Seq and CLIP-seq transcriptomic profiles with limma (limma-voom) (Smyth, 2005) (Galaxy Version 3.58.1+galaxy0).

The peaks detected with PEAKachu were further filtered and annotated. We first removed peaks for which expression in the RNA-Seq was null (noted Inf by PEAKachu). For annotation, we used the BioMart tool (Smedley et al., 2009) to extract coordinates, strand for canonical transcripts of the mouse genome annotation. We then only kept peaks overlapping annotated exons on the same strand with IntersectBed for the Bedtools suite (Quinlan and Hall, 2010). We further kept peaks overlapping genes found over-expressed in the CLIP-Seq dataset when compared to the RNA-Seq dataset (with limma).

To convert the RNA sequence under the peaks, we used the R package geno2proteo (Li et al., 2019). We then counted the frequency each amino acid under the remaining peaks (**Supplemental Table S2**).

References

Afgan E et al. (2018) The Galaxy platform for accessible, reproducible and collaborative biomedical analyses: 2018 update. Nucleic Acids Res 46:W537–W544.

Aguilar Rangel M, Stein K, Frydman J (2024) A machine learning approach uncovers principles and determinants of eukaryotic ribosome pausing. Sci Adv 10:eado0738.

Almena M, Merida I (2011) Shaping up the membrane: diacylglycerol coordinates spatial orientation of signaling. Trends Biochem Sci 36:593–603.

Anadolu MN, Sun J, Kailasam S, Chalkiadaki K, Krimbacher K, Li JT-Y, Markova T, Jafarnejad SM, Lefebvre F, Ortega J, Gkogkas CG, Sossin WS (2023) Ribosomes in RNA Granules Are Stalled on mRNA Sequences That Are Consensus Sites for FMRP Association. J Neurosci 43:2440–2459.

Anon (1994) The Dutch-Belgian Fragile X Consortium. Cell 78:23–33.

Arguello AE, DeLiberto AN, Kleiner RE (2017) RNA Chemical Proteomics Reveals the N6-Methyladenosine (m6A)-Regulated Protein-RNA Interactome. J Am Chem Soc 139:17249–17252.

Arpat AB, Liechti A, De Matos M, Dreos R, Janich P, Gatfield D (2020) Transcriptome-wide sites of collided ribosomes reveal principles of translational pausing. Genome Res 30:985–999.

Ascano M Jr, Mukherjee N, Bandaru P, Miller JB, Nusbaum JD, Corcoran DL, Langlois C, Munschauer M, Dewell S, Hafner M, Williams Z, Ohler U, Tuschl T (2012) FMRP targets distinct mRNA sequence elements to regulate protein expression. Nature 492:382–386.

Aviner R, Lee T-T, Masto VB, Li KH, Andino R, Frydman J (2024) Polyglutamine-mediated ribotoxicity disrupts proteostasis and stress responses in Huntington's disease. Nat Cell Biol 26:892–902.

Bear MF, Huber KM, Warren ST (2004) The mGluR theory of fragile X mental retardation. Trends Neurosci 27:370–377.

Biever A, Valjent E, Puighermanal E (2015) Ribosomal Protein S6 Phosphorylation in the Nervous System: From Regulation to Function. Front Mol Neurosci 8:75.

Bolger AM, Lohse M, Usadel B (2014) Trimmomatic: a flexible trimmer for Illumina sequence data. Bioinformatics 30:2114–2120.

Chang M, Lv H, Zhang W, Ma C, He X, Zhao S, Zhang Z-W, Zeng Y-X, Song S, Niu Y, Tong W-M (2017) Region-specific RNA m6A methylation represents a new layer of control in the gene regulatory network in the mouse brain. Open Biol 7:170166.

Chen L, Yun SW, Seto J, Liu W, Toth M (2003) The fragile X mental retardation protein binds and regulates a novel class of mRNAs containing U rich target sequences. Neuroscience 120:1005–1017.

Choi J, Ieong K-W, Demirci H, Chen J, Petrov A, Prabhakar A, O'Leary SE, Dominissini D, Rechavi G, Soltis SM, Ehrenberg M, Puglisi JD (2016) N6-methyladenosine in mRNA disrupts tRNA selection and translation elongation dynamics. Nat Struct Mol Biol 23:110–115.

Chyżyńska K, Labun K, Jones C, Grellscheid SN, Valen E (2021) Deep conservation of ribosome stall sites across RNA processing genes. NAR Genom Bioinform 3:lqab038.

Cooke M, Kazanietz MG (2022) Overarching roles of diacylglycerol signaling in cancer development and antitumor immunity. Sci Signal 15:eabo0264.

Crabbe LS, Bensky AS, Hornstein L, Schwartz DC (1993) Cardiovascular abnormalities in children with fragile X syndrome. Pediatrics 91:714–715.

Darnell JC, Fraser CE, Mostovetsky O, Stefani G, Jones TA, Eddy SR, Darnell RB (2005) Kissing complex RNAs mediate interaction between the Fragile-X mental retardation protein KH2 domain and brain polyribosomes. Genes Dev 19:903–918.

Darnell JC, Jensen KB, Jin P, Brown V, Warren ST, Darnell RB (2001) Fragile X mental retardation protein targets G quartet mRNAs important for neuronal function. Cell 107:489–499.

Darnell JC, Klann E (2013) The translation of translational control by FMRP: therapeutic targets for FXS. Nat Neurosci 16:1530–1536.

Darnell JC, Van Driesche SJ, Zhang C, Hung KYS, Mele A, Fraser CE, Stone EF, Chen C, Fak JJ, Chi SW, Licatalosi DD, Richter JD, Darnell RB (2011) FMRP Stalls Ribosomal Translocation on mRNAs Linked to Synaptic Function and Autism. Cell 146:247–261.

Darnell JC, Warren ST, Darnell RB (2004) The fragile X mental retardation protein, FMRP, recognizes G-quartets. Ment Retard Dev Disabil Res Rev 10:49–52.

Dictenberg JB, Swanger SA, Antar LN, Singer RH, Bassell GJ (2008) A direct role for FMRP in activity-dependent dendritic mRNA transport links filopodial-spine morphogenesis to fragile X syndrome. Dev Cell 14:926–939.

Dobin A, Davis CA, Schlesinger F, Drenkow J, Zaleski C, Jha S, Batut P, Chaisson M, Gingeras TR (2013) STAR: ultrafast universal RNA-seq aligner. Bioinformatics 29:15–21.

Dölen G, Osterweil E, Rao BSS, Smith GB, Auerbach BD, Chattarji S, Bear MF (2007) Correction of fragile X syndrome in mice. Neuron 56:955–962.

Dolzhanskaya N, Sung YJ, Conti J, Currie JR, Denman RB (2003) The fragile X mental retardation protein interacts with U-rich RNAs in a yeast three-hybrid system. Biochem Biophys Res Commun 305:434–441.

Edens BM, Vissers C, Su J, Arumugam S, Xu Z, Shi H, Miller N, Rojas Ringeling F, Ming G-L, He C, Song H, Ma YC (2019) FMRP Modulates Neural Differentiation through m6A-Dependent mRNA Nuclear Export. Cell Rep 28:845-854.e5.

Edupuganti RR, Geiger S, Lindeboom RGH, Shi H, Hsu PJ, Lu Z, Wang S-Y, Baltissen MPA, Jansen PWTC, Rossa M, Müller M, Stunnenberg HG, He C, Carell T, Vermeulen M (2017) N(6)-methyladenosine (m(6)A) recruits and repels proteins to regulate mRNA homeostasis. Nat Struct Mol Biol 24:870–878.

Eichmann TO, Lass A (2015) DAG tales: the multiple faces of diacylglycerol--stereochemistry, metabolism, and signaling. Cell Mol Life Sci 72:3931–3952.

Flamand MN, Meyer KD (2022) m6A and YTHDF proteins contribute to the localization of select neuronal mRNAs. Nucleic Acids Res 50:4464–4483.

Gaskill BN, Gordon CJ, Pajor EA, Lucas JR, Davis JK, Garner JP (2013) Impact of nesting material on mouse body temperature and physiology. Physiol Behav 110–111:87–95.

George J et al. (2021) RNA-binding protein FXR1 drives cMYC translation by recruiting eIF4F complex to the translation start site. Cell Rep 37:109934.

Gessulat S, Schmidt T, Zolg DP, Samaras P, Schnatbaum K, Zerweck J, Knaute T, Rechenberger J, Delanghe B, Huhmer A, Reimer U, Ehrlich H-C, Aiche S, Kuster B, Wilhelm M (2019) Prosit: proteome-wide prediction of peptide tandem mass spectra by deep learning. Nat Methods 16:509–518.

Greenblatt EJ, Spradling AC (2018) Fragile X mental retardation 1 gene enhances the translation of large autism-related proteins. Science 361:709–712.

Gutierrez E, Shin B-S, Woolstenhulme CJ, Kim J-R, Saini P, Buskirk AR, Dever TE (2013) eIF5A promotes translation of polyproline motifs. Mol Cell 51:35–45.

Hafner M, Landthaler M, Burger L, Khorshid M, Hausser J, Berninger P, Rothballer A, Ascano M, Jungkamp A-C, Munschauer M, Ulrich A, Wardle GS, Dewell S, Zavolan M, Tuschl T (2010) Transcriptome-wide Identification of RNA-Binding Protein and MicroRNA Target Sites by PAR-CLIP. Cell 141:129–141.

Hagerman RJ, Berry-Kravis E, Hazlett HC, Bailey DB, Moine H, Kooy RF, Tassone F, Gantois I, Sonenberg N, Mandel JL, Hagerman PJ (2017) Fragile X syndrome. Nat Rev Dis Primers 3:17065.

Hagerman RJ, Synhorst DP (1984) Mitral valve prolapse and aortic dilatation in the fragile X syndrome. Am J Med Genet 17:123–131.

Han P, Shichino Y, Schneider-Poetsch T, Mito M, Hashimoto S, Udagawa T, Kohno K, Yoshida M, Mishima Y, Inada T, Iwasaki S (2020) Genome-wide Survey of Ribosome Collision. Cell Rep 31:107610.

Hardiman RL, Bratt A (2016) Hypothalamic-pituitary-adrenal axis function in Fragile X Syndrome and its relationship to behaviour: A systematic review. Physiology & Behavior 167:341–353.

He CX, Portera-Cailliau C (2013) The trouble with spines in fragile X syndrome: density, maturity and plasticity. Neuroscience 251:120–128.

Heyl F, Maticzka D, Batut B (2026) CLIP-Seq data analysis from pre-processing to motif detection (Galaxy Training Materials). Available at: https://training.galaxyproject.org/training-material/topics/transcriptomics/tutorials/clipseq/tutorial.html.

Hsu PJ, Shi H, Zhu AC, Lu Z, Miller N, Edens BM, Ma YC, He C (2019) The RNA-binding protein FMRP facilitates the nuclear export of N6-methyladenosine-containing mRNAs. J Biol Chem 294:19889–19895.

Huppertz I, Attig J, D'Ambrogio A, Easton LE, Sibley CR, Sugimoto Y, Tajnik M, König J, Ule J (2014) iCLIP: Protein–RNA interactions at nucleotide resolution. Methods 65:274–287.

Ichihara K, Shiraishi T, Chadani Y, Kito Y, Shiraishi C, Hirata M, Takahashi Y, Kobo A, Hatano A, Matsumoto M, Machida K, Imataka H, Toyoda A, Mishiro-Sato E, Nojima T, Ito T, Taguchi H, Nakayama KI, Matsumoto A (2025) eIF2D promotes 40S ribosomal subunit recycling during intrinsic ribosome destabilization. Nucleic Acids Research 53:gkaf1322.

Imai S, Kai M, Yasuda S, Kanoh H, Sakane F (2005) Identification and characterization of a novel human type II diacylglycerol kinase, DGK kappa. J Biol Chem 280:39870–39881.

Ito Y, Chadani Y, Niwa T, Yamakawa A, Machida K, Imataka H, Taguchi H (2022) Nascent peptide-induced translation discontinuation in eukaryotes impacts biased amino acid usage in proteomes. Nat Commun 13:7451.

Kan L, Ott S, Joseph B, Park ES, Dai W, Kleiner RE, Claridge-Chang A, Lai EC (2021) A neural m6A/Ythdf pathway is required for learning and memory in Drosophila. Nat Commun 12:1458.

Kao D-I, Aldridge GM, Weiler IJ, Greenough WT (2010) Altered mRNA transport, docking, and protein translation in neurons lacking fragile X mental retardation protein. Proceedings of the National Academy of Sciences 107:15601–15606.

Kazdoba TM, Leach PT, Silverman JL, Crawley JN (2014) Modeling fragile X syndrome in the Fmr1 knockout mouse. Intractable Rare Dis Res 3:118–133.

Kim K, Yang J, Zhong XP, Kim MH, Kim YS, Lee HW, Han S, Choi J, Han K, Seo J, Prescott SM, Topham MK, Bae YC, Koretzky G, Choi SY, Kim E (2009) Synaptic removal of diacylglycerol by DGKzeta and PSD-95 regulates dendritic spine maintenance. Embo J 28:1170–1179.

Kong J, Lasko P (2012) Translational control in cellular and developmental processes. Nat Rev Genet 13:383–394.

Leboucher A, Bermudez-Martin P, Mouska X, Amri E-Z, Pisani DF, Davidovic L (2019a) Fmr1-Deficiency Impacts Body Composition, Skeleton, and Bone Microstructure in a Mouse Model of Fragile X Syndrome. Front Endocrinol (Lausanne) 10:678.

Leboucher A, Pisani DF, Martinez-Gili L, Chilloux J, Bermudez-Martin P, Van Dijck A, Ganief T, Macek B, Becker JAJ, Le Merrer J, Kooy RF, Amri E-Z, Khandjian EW, Dumas M-E, Davidovic L (2019b) The translational regulator FMRP controls lipid and glucose metabolism in mice and humans. Mol Metab 21:22–35.

Lee D, Kim E, Tanaka-Yamamoto K (2016) Diacylglycerol Kinases in the Coordination of Synaptic Plasticity. Front Cell Dev Biol 4:92.

Lee Y, Choe J, Park OH, Kim YK (2020) Molecular Mechanisms Driving mRNA Degradation by m6A Modification. Trends in Genetics 36:177–188.

Li JT-Y, Amiri M, Kailasam S, Sun J, Sonenberg N, Ortega J, Sossin WS (2025) FMRP Regulates Neuronal RNA Granules Containing Stalled Ribosomes, Not Where Ribosomes Stall. Available at: http://dx.doi.org/10.7554/eLife.106692.1.

Li Y, Aguilar-Martinez E, Sharrocks AD (2019) Geno2proteo, a Tool for Batch Retrieval of DNA and Protein Sequences from Any Genomic or Protein Regions. J Integr Bioinform 16:20180090.

Li Z, Zhang Y, Ku L, Wilkinson KD, Warren ST, Feng Y (2001) The fragile X mental retardation protein inhibits translation via interacting with mRNA. Nucleic Acids Res 29:2276–2283.

Liao Y, Smyth GK, Shi W (2014) featureCounts: an efficient general purpose program for assigning sequence reads to genomic features. Bioinformatics 30:923–930.

Linder B, Sharma P, Wu J, Birbaumer T, Eggers C, Murakami S, Ott RE, Fenzl K, Vorgerd H, Erhard F, Jaffrey SR, Leidel SA, Steinmetz LM (2025) tRNA modifications tune m(6)A-dependent mRNA decay. Cell 188:3715-3727.e13.

Loedige I, Baranovskii A, Mendonsa S, Dantsuji S, Popitsch N, Breimann L, Zerna N, Cherepanov V, Milek M, Ameres S, Chekulaeva M (2023) mRNA stability and m6A are major determinants of subcellular mRNA localization in neurons. Molecular Cell 83:2709-2725.e10.

Loehr JP, Synhorst DP, Wolfe RR, Hagerman RJ (1986) Aortic root dilatation and mitral valve prolapse in the fragile X syndrome. Am J Med Genet 23:189–194.

Long J-Y, Jiang W, Xia H-B, Fu J-Y, Lu P, Hu F, Feng W-C, Sun W-W, Gao M-M, Yi Y-H, Long Y-S (2020) FMRP-absence-induced up-regulation of hypothalamic MAP1B expression decreases AgRP level linking with reduces in food intake and body weight. Neurochemistry International 140:104847.

Mao Y, Dong L, Liu X-M, Guo J, Ma H, Shen B, Qian S-B (2019) m(6)A in mRNA coding regions promotes translation via the RNA helicase-containing YTHDC2. Nat Commun 10:5332.

Maurin T, Lebrigand K, Castagnola S, Paquet A, Jarjat M, Popa A, Grossi M, Rage F, Bardoni B (2018) HITS-CLIP in various brain areas reveals new targets and new modalities of RNA binding by fragile X mental retardation protein. Nucleic Acids Res 46:6344–6355.

Mérida I, Avila-Flores A, Merino E (2008) Diacylglycerol kinases: at the hub of cell signalling. Biochem J 409:1–18.

Mientjes EJ, Nieuwenhuizen I, Kirkpatrick L, Zu T, Hoogeveen-Westerveld M, Severijnen L, Rifé M, Willemsen R, Nelson DL, Oostra BA (2006) The generation of a conditional *Fmr1* knock out mouse model to study Fmrp function in vivo. Neurobiology of Disease 21:549–555.

Moine H, Vitale N (2019) Of local translation control and lipid signaling in neurons. Adv Biol Regul 71:194–205.

Murakami S, Jaffrey SR (2022) Hidden codes in mRNA: Control of gene expression by m6A. Mol Cell 82:2236–2251.

Murakami S, Olarerin-George AO, Liu JF, Zaccara S, Hawley B, Jaffrey SR (2025) m6A alters ribosome dynamics to initiate mRNA degradation. Cell 188:3728-3743.e20.

Muzar Z, Lozano R, Kolevzon A, Hagerman RJ (2016) The neurobiology of the Prader-Willi phenotype of fragile X syndrome. Intractable Rare Dis Res 5:255–261.

Nowicki ST, Tassone F, Ono MY, Ferranti J, Croquette MF, Goodlin-Jones B, Hagerman RJ (2007) The Prader-Willi phenotype of fragile X syndrome. J Dev Behav Pediatr 28:133–138.

Pyeritz RE, Stamberg J, Thomas GH, Bell BB, Zahka KG, Bernhardt BA (1982) The marker Xq28 syndrome ("Fragile-X SYndrome") in a retarded man with mitral valve prolapse. Johns Hopkins Med J 151:231–237.

Qin M, Kang J, Burlin TV, Jiang C, Smith CB (2005) Postadolescent changes in regional cerebral protein synthesis: an in vivo study in the FMR1 null mouse. J Neurosci 25:5087–5095.

Quinlan AR, Hall IM (2010) BEDTools: a flexible suite of utilities for comparing genomic features. Bioinformatics 26:841–842.

Richard MA, Sok P, Canon S, Brown AL, Peckham-Gregory EC, Nembhard WN, Carmichael SL, Ehli EA, Kallsen NA, Peyton SA, Davies GE, Patel A, Zamilpa I, Wyatt RA, Hobbs CA, Scheurer ME, Lupo PJ (2019) The role of genetic variation in DGKK on moderate and severe hypospadias. Birth Defects Res 111:932–937.

Ruggiero-Ruff RE, Villa PA, Hijleh SA, Avalos B, DiPatrizio NV, Haga-Yamanaka S, Coss D (2023) Increased body weight in mice with fragile X messenger ribonucleoprotein 1 (Fmr1) gene mutation is associated with hypothalamic dysfunction. Sci Rep 13:12666.

Schaeffer C, Bardoni B, Mandel JL, Ehresmann B, Ehresmann C, Moine H (2001) The fragile X mental retardation protein binds specifically to its mRNA via a purine quartet motif. Embo J 20:4803–4813.

Shafik AM, Zhang F, Guo Z, Dai Q, Pajdzik K, Li Y, Kang Y, Yao B, Wu H, He C, Allen EG, Duan R, Jin P (2021) N6-methyladenosine dynamics in neurodevelopment and aging, and its potential role in Alzheimer's disease. Genome Biol 22:17.

Shirai Y, Kouzuki T, Kakefuda K, Moriguchi S, Oyagi A, Horie K, Morita SY, Shimazawa M, Fukunaga K, Takeda J, Saito N, Hara H (2010) Essential role of neuron-enriched diacylglycerol kinase (DGK), DGKbeta in neurite spine formation, contributing to cognitive function. PLoS One 5:e11602.

Siomi MC, Zhang Y, Siomi H, Dreyfuss G (1996) Specific sequences in the fragile X syndrome protein FMR1 and the FXR proteins mediate their binding to 60S ribosomal subunits and the interactions among them. Mol Cell Biol 16:3825–3832.

Smedley D, Haider S, Ballester B, Holland R, London D, Thorisson G, Kasprzyk A (2009) BioMart--biological queries made easy. BMC Genomics 10:22.

Smyth GK (2005) Limma: linear models for microarray data. In: "Bioinformatics and Computational Biology Solutions using R and Bioconductor."

Sreeram N, Wren C, Bhate M, Robertson P, Hunter S (1989) Cardiac abnormalities in the fragile X syndrome. British heart journal 61:289—291.

Suhl JA, Chopra P, Anderson BR, Bassell GJ, Warren ST (2014) Analysis of FMRP mRNA target datasets reveals highly associated mRNAs mediated by G-quadruplex structures formed via clustered WGGA sequences. Hum Mol Genet 23:5479–5491.

Tabet R Tabet R, Moutin E, Becker JA, Heintz D, Fouillen L, Flatter E, Krężel W, Alunni V, Koebel P, Dembélé D, Tassone F, Bardoni B, Mandel JL, Vitale N, Muller D, Le

Merrer J, Moine H (2016a) Fragile X Mental Retardation Protein (FMRP) controls diacylglycerol kinase activity in neurons. Proc Natl Acad Sci U S A.113(26):E3619-28.

Tabet R, Vitale N, Moine H (2016b) Fragile X syndrome: Are signaling lipids the missing culprits? Biochimie Available at: http://www.ncbi.nlm.nih.gov/pubmed/27597551.

Tarasov A, Vilella AJ, Cuppen E, Nijman IJ, Prins P (2015) Sambamba: fast processing of NGS alignment formats. Bioinformatics 31:2032–2034.

Uematsu S, Qian S-B (2025) Interpreting ribosome dynamics during mRNA translation. J Biol Chem 301:110469.

van der Zanden LFM, van Rooij IALM, Feitz WFJ, Knight J, Donders ART, Renkema KY, Bongers EMHF, Vermeulen SHHM, Kiemeney LALM, Veltman JA, Arias-Vásquez A, Zhang X, Markljung E, Qiao L, Baskin LS, Nordenskjöld A, Roeleveld N, Franke B, Knoers NVAM (2011) Common variants in DGKK are strongly associated with risk of hypospadias. Nat Genet 43:48–50.

Veltri AJ, D'Orazio KN, Lessen LN, Loll-Krippleber R, Brown GW, Green R (2022) Distinct elongation stalls during translation are linked with distinct pathways for mRNA degradation Hinnebusch AG, Manley JL, eds. eLife 11:e76038.

Worpenberg L et al. (2021) Ythdf is a N6-methyladenosine reader that modulates Fmr1 target mRNA selection and restricts axonal growth in Drosophila. EMBO J 40:e104975.

Yang J, Seo J, Nair R, Han S, Jang S, Kim K, Han K, Paik SK, Choi J, Lee S, Bae YC, Topham MK, Prescott SM, Rhee JS, Choi SY, Kim E (2011) DGKiota regulates presynaptic release during mGluR-dependent LTD. Embo J 30:165–180.

Zambo B, Morlet B, Negroni L, Trave G, Gogl G (2022) Native holdup (nHU) to measure binding affinities from cell extracts. Science advances 8 Available at: https://pubmed-ncbi-nlm-nih-gov.proxy.insermbiblio.inist.fr/36542723/ [Accessed June 19, 2024].

Zeisel A et al. (2018) Molecular Architecture of the Mouse Nervous System. Cell 174:999-1014.e22.

Zhang G, Xu Y, Wang X, Zhu Y, Wang L, Zhang W, Wang Y, Gao Y, Wu X, Cheng Y, Sun Q, Chen D (2022) Dynamic FMR1 granule phase switch instructed by m6A modification contributes to maternal RNA decay. Nat Commun 13:859.

Zhang Y, Glineburg MR, Basrur V, Conlon K, Wright SE, Krans A, Hall DA, Todd PK (2022) Mechanistic convergence across initiation sites for RAN translation in fragile X associated tremor ataxia syndrome. Hum Mol Genet 31:2317–2332.

Zhao T, Chen Y-M, Li Y, Wang J, Chen S, Gao N, Qian W (2021) Disome-seq reveals widespread ribosome collisions that promote cotranslational protein folding. Genome Biol 22:16.

Zhou Y, Ćorović M, Hoch-Kraft P, Meiser N, Mesitov M, Körtel N, Back H, Naarmann-de Vries IS, Katti K, Obrdlík A, Busch A, Dieterich C, Vaňáčová Š, Hengesbach M,

Zarnack K, König J (2024) m6A sites in the coding region trigger translation-dependent mRNA decay. Mol Cell 84:4576-4593.e12.

Zou Z, Wei J, Chen Y, Kang Y, Shi H, Yang F, Shi Z, Chen S, Zhou Y, Sepich-Poore C, Zhuang X, Zhou X, Jiang H, Wen Z, Jin P, Luo C, He C (2023) FMRP phosphorylation modulates neuronal translation through YTHDF1. Mol Cell 83:4304-4317.e8.

Acknowledgments:

We thank Marie-Christine Birling and the members of the Institut Clinique de la Souris for their assistance in creating the DGKk-KO model and conducting behavioral studies. We are grateful to Sirine Souali-crespo for her support in anatomical studies. We extend our thanks to Bernard Jost and Stephanie Legras for their guidance with RNA sequencing and analyses, Erwan Grandgirard for imaging support, and Bastien Morlet for his help with PRM studies. Our appreciation also goes to Nicolas Zerbe and the IGBMC core facilities for their technical assistance. We are especially grateful to Nicolas Charlet-Berguerand and Frank Martin for their insightful discussions and suggestions. Finally, we wish to thank our colleagues in the TMN department for their support and interest throughout this work.

Funding:

This work was supported by Fondation Jérôme Lejeune funding and StrasND to HM, by Fragile X France to OK and Fondation pour la Recherche Médicale to BZ. This study was also supported by Interdisciplinary Thematic Institute IMCBio+ 2021-2028 program of the University of Strasbourg, CNRS, and Inserm, through IdEx Unistra (ANR-10-IDEX-0002) and EUR IMCBio (ANR-17-EURE-0023) under the France 2030 Program framework.

Author contributions

OC, BZ, LN designed and performed experiments and helped writing the manuscript. ND, AP, BJ performed statistical analyses. GG, AP helped designing the experiments and writing manuscript. TM designed and performed bioinformatic analyses. HM supervised the project, designed experiments and wrote the manuscript.

Competing interests

HM is listed as inventor on a patent describing the use of DGKκ for FXS therapy. All other authors declare no competing interests.

Figure legends:

Figure 1: FXRs bind *Dgkk* mRNA with high affinity across the brain and positively regulate its translation

A) Single-molecule–resolution spatial transcriptomic MERFISH data (Vizgen) showing *Dgkk* mRNA (blue) in mouse brain coronal sections. Upper panel: 3D reconstruction generated from 67 MERFISH sections.

B) Single-cell transcriptomic (Zeisel et al., 2018) reanalysis showing the expression patterns of DGKs across major brain cell types.

C) qRT–PCR analysis of *Dgkk* expression in primary cortical and hypothalamic neurons at DIV8. Relative expression levels were calculated using the ΔΔCT method with *Rplp0* as the housekeeping gene. Data are presented as mean ± SEM and were analyzed using an unpaired Student's t-test. ****$P < 0.0001$.

D–E) CLIP–qPCR analysis of FMRP in primary D) cortical and E) hypothalamic neurons at DIV8. Bar graphs represent IP/Input enrichment relative to the Map1b signal. Established FMRP mRNA targets (*Map1b* and *Psd95*) and a non-target control (*Rplp0*) were included to assess specificity. Analysis in *Fmr1*-KO neurons confirms immunoprecipitation specificity. Each dot represents an independent culture.

F) qRT–PCR analysis of *Dgkk* expression in cortex, hippocampus, hypothalamus, thalamus, pituitary gland, and pons from adult WT and *Fmr1*-KO mice. Fold changes were calculated using the ΔΔCt method with Tbp as the housekeeping gene. Data are mean ± SEM and were analyzed using multiple t-tests comparing expression in WT and *Fmr1*-KO across brain regions.

G) PRM-targeted proteomic quantification of DGKκ in cortex and hypothalamus from WT and *Fmr1*-KO mice. Each dot represents an individual mouse. Data are mean ± SEM and were analyzed using an unpaired Student's t-test. **P < 0.01.

H) Representative western blots of FMRP and FXR1P in cortex and hypothalamus. Quantification was normalized to GAPDH and expressed relative to cortex expression. Data are mean ± SEM and were analyzed using unpaired Student's t-tests. **P < 0.01.

I) CLIP–qPCR analysis of FXR1P in primary hypothalamic neurons at DIV8. Bar graphs represent IP/Input enrichment relative to the Map1b signal. An established FXR1P target (*cMyc*) was used as a positive control, while Rplp0 and Actb served as non-target controls.

Figure 2: *Dgkk*-KO mice exhibit FXS-like and overgrowth phenotypes.

A) Open field test. Total distance traveled over 30 min and percentage of time spent in the center of the arena. Data are mean ± SEM and were analyzed using unpaired Student's t-tests. *P<0.05; ***P < 0.001.

B) Marble burying test. Number of marbles buried within 15 min, indicative of compulsive-like behavior and/or hyperactivity. Data are presented as mean ± SEM and analyzed by two-way repeated-measures ANOVA to evaluate the overall effect of genotype.

C) Social interaction test. Frequency of interactions between the test mouse and a novel conspecific. Data are mean ± SEM and were analyzed using unpaired Student's t-tests. *P<0.05.

D) Acoustic startle response. Amplitude of the startle reflex elicited by an acoustic stimulus. Each dot represents one mouse. Data are mean ± SEM and were analyzed using unpaired Student's t-tests. **P<0.001.

E) Body weight of WT and *Dgkk*-KO mice measured across multiple ages, with representative images of WT and *Dgkk*-KO mice (scale bar, 1 cm). Data are presented as

mean ± SEM and analyzed by two-way repeated-measures ANOVA to evaluate the overall effect of genotype. ***P < 0.001.

F) Body size of 13-week-old WT and *Dgkk*-KO mice.

G–I) Quantitative NMR (qNMR) body composition analysis showing G) fat mass, H) lean mass, and I) free body fluid mass. Data are mean ± SEM and were analyzed using unpaired Student's t-tests. *P<0.05; ***P<0.001.

J) Bone density measurements. Data are mean ± SEM and were analyzed using unpaired Student's t-tests. *P<0.05.

K–L) Echocardiographic assessment of K) heart mass and L) left ventricular mass. Each dot represents one mouse. Data are mean ± SEM and were analyzed using unpaired Student's t-tests. **P<0.01; ***P<0.001.

Figure 3: DGKκ loss results in dendritic spines morphology and mGluRI-dependent activity alterations, and aberrant DAG-signaling leading to increased neuronal translational rate

A) Neuronal localization of HA-DGKκ (fire) in primary hippocampal neurons and its colocalization with the synaptic marker PSD95 (green) at 17 DIV. Hippocampal neurons were magnetofected at 3 DIV with HA-tagged DGKκ constructs. At 17 DIV, neurons were immunolabeled with antibodies against HA and PSD95. Images were acquired by confocal microscopy. Digital magnification shows colocalization of DGKκ with PSD95 in dendritic spines. CB: cell body; Sp: spine. Scale bar: 30 µm.

B) Ribopuromycylation assay in hippocampal neurons at DIV17. Top panel: no puromycin control. Bottom panel: arrows indicate colocalization of DGKκ (fire) with puromycin signal (white), highlighting sites of active translation. Scale bar: 2 µm.

C) Quantification and classification of dendritic spine morphology in magnetofected GFP-positive hippocampal neurons at 21 DIV from WT and *Dgkk*-KO mice. Upper panel: representative 3D reconstructions of dendritic spine morphology for each condition. Spine analysis was performed using Imaris on GFP-labeled neurons, analyzing 100–200 spines per 8–10 neurons per biological replicate. Data are presented as mean ± SEM and analyzed using two-way ANOVA followed by Sidak's multiple-comparisons test. *P < 0.05; **P < 0.01.

D) MEA recordings. Upper panel: raster plot example in which each line represents a different electrode (subset shown) and each dot represents an above-threshold spiking event. Lower panel: mGluRI-dependent activity in WT and *Dgkk*-KO cortical neurons measured before and after 1 min of treatment with 100 µM DHPG. Each dot represents data from an individual embryo. Data are mean ± SEM and analyzed using paired Student's t-test. *P < 0.05; **P < 0.01.

E) Representative western blots of lysates from WT and *Dgkk*-KO cortical neurons at 7 DIV and quantification of phosphorylation and total levels of indicated proteins. GAPDH was used as a loading control. Phospho-protein signals were normalized to total protein and expressed relative to WT. Data are mean ± SEM and were analyzed using unpaired Student's t-tests. **P<0.01; ****P<0.0001.

F) Representative western blots of puromycin-labeled neuron lysates from WT and *Dgkk*-KO cortical neurons treated for 30 min with 20 µg/mL puromycin. Puromycin signals were normalized to GAPDH and expressed relative to WT. Each dot represents an individual culture. Data are mean ± SEM and were analyzed using unpaired Student's t-tests. **P<0.01.

Figure 4: FMRP binds the m^{6}A modified EPAP motif of *Dgkk* mRNA and mitigates ribosomal stalling imposed by the sequence.

A) IGV representation of *Dgkk* mRNA showing HITS-CLIP-seq profiles of FMRP (upper tracks) and m□A-seq profiles (lower tracks) from hypothalamic neurons, relative to input (Shafik et al., 2021). Sequence logo analysis of conserved FMRP binding sites in mouse and human DGKκ.

B) CLIP-qPCR in HeLa cells for Nter-DGKκ-Nluc and ΔEPAP-Nluc constructs. Bars represent IP/Input relative enrichment. A non-target control (GAPDH) was included to assess specificity. Each dot represents an independent culture.

C) Representative western blot of transfected WT DGKκ and ΔNter DGKκ tagged with HA in HeLa cells. GAPDH was used as a loading control.

D–E) Sucrose gradient control shows ribosome profile of undigested and RNase-A-digested lysate. Northern blot analysis of RNase-A–digested ribosomal footprints. Specific radio-labeled probes for NLuc (D) and EPAP (E) were used. For emetine-positive control, cells were incubated with 2 μM emetine for 15 min prior to lysis. Ethidium bromide staining was used as a loading control.

F) Luciferase assays of indicated NLuc constructs in WT and *Fmr1*-KO cortical primary neurons at DIV4. Firefly luciferase was used as a normalization control. Data are mean ± SEM and analyzed using multiple t-tests comparing enrichment in WT and *Fmr1*-KO for each gene. ***$P < 0.001$.

G) CLIP–qPCR analysis of FMRP in cortical neurons treated with Acell siRNA control or siRNA targeting *Mettl3*. Bars represent IP/Input enrichment relative to Map1b signal. Well-established FMRP targets (*Map1b*, *Psd95*), non-target controls (*Rplp0*), an m^6A-containing FMRP target (*Cdk5r1*), and a non-target (*Bdnf*) were included for specificity assessment. Each dot represents an independent culture. Data are mean ± SEM and analyzed using multiple t-tests comparing enrichment in WT and *Fmr1*-KO for each gene. **$P < 0.01$.

H) RNA pull-down proteomic analysis using immobilized EPAP RNA probes with or without m^6A modification, incubated with WT neuronal lysate. P-values were calculated using a two-sided unpaired t test, and statistical thresholds for binding (dotted lines) were determined at 1 standard deviation and P-value < 0.05.

I) Translation efficiency measurement of indicated constructs in HeLa cells transfected with control or *METTL3*-targeting siRNA. Luciferase signals were normalized to RNA levels of the corresponding constructs. Data are mean ± SEM and analyzed using multiple t-tests comparing enrichment in WT and *Fmr1*-KO for each gene. *P<0.05; ***P < 0.001.

J) Hydrophobicity versus frequency of enriched tripeptides identified in FMRP-bound peptide sequences. Scatter plot showing the enrichment of unordered tripeptide motifs detected in amino-acid sequences derived from FMRP CLIP–enriched transcripts. Tripeptides were scanned in sliding windows of 30 amino acids, and motifs detected ≥2 times within the same window were collapsed into non-ordered compositions (e.g., EPE/PEE/EEP → "EEP"). The y-axis reports the fraction of enriched windows containing each motif across all FMRP-associated sequences. The x-axis shows the mean Kyte–Doolittle hydrophobicity, plotted on an inverted scale to distinguish hydrophobic (left) from hydrophilic (right) motifs; the dashed vertical line marks hydrophobicity 0. Point color indicates net charge (K/R: +1; D/E: –1), and selected motifs with high co-occurrence or extreme hydrophobicity are labelled.

K) Proposed model for the coordinated action of FMRP and m^6A on amino acid clusters that alter translational elongation kinetics.

<u>Supplementary figure legends:</u>

Figure S1: Validation of FMRP immunoprecipitation and expression of FXRs in the mouse brain

A) Validation of FMRP immunoprecipitation in cortical neurons using an FMRP-specific antibody. *Fmr1*-KO neurons and IgG antibodies were used as negative controls.

B) Expression pattern of FXR proteins in the mouse brain. Data obtained from www.proteinatlas.org.

Figure S2: Behavioral analyses and echocardiography of *Dgkk*-KO mice

A) RT-PCR analysis of exons 1–4 and 8–9 of the *Dgkk* gene in WT and *Dgkk*-KO mice. *Gapdh* RT-PCR was used as a loading control.

B) Western blot of hypothalamic lysates from WT and *Dgkk*-KO mice using a partially DGKκ-specific antibody.

C–D) Detection and quantification of a DGKκ-specific peptide by targeted proteomics in hypothalamic lysates from WT and *Dgkk*-KO mice. C) Representative detection. D) Quantification of DGKκ-specific peptide levels.

E) qRT-PCR analysis of 9 Dgk isoforms and *Psd95* in WT and *Dgkk*-KO mouse brains. Data are presented as mean fold change ± SEM and analyzed using unpaired Student's t-test. ***P<0.001.

F) Dissection of WT and *Dgkk*-KO mice penis indicates the absence of urogenital abnormalities.

G-I) Elevated plus maze test. Preferential exploration of G) open arms versus H) closed arms in a "+"-shaped maze. I) Total arm entries were counted to assess general locomotor activity.

J) Percentage of time spent in open arms, reflecting anxiety-like behavior, was calculated.

K–M) Novel object recognition test. K) Exploration duration during the acquisition phase. L) Exploration duration during the retention phase. M) Recognition index calculated to assess episodic memory.

N) Nest-building assay. Nests were scored at 2, 5, and 24 h using a 0–5 scale as described by (Gaskill et al., 2013): 0 = undisturbed nesting material; 1 = disturbed material but no nest site; 2 = flat nest without walls; 3 = cup nest with wall < ½ the height of a dome; 4 = incomplete dome with wall ½ the height of a dome; 5 = complete dome with walls > ½ the height of a dome, which may or may not fully enclose the nest.

O–P) Echocardiography measurement of left ventricular blood volume during O) diastole and P) systole. Data are presented as mean ± SEM and analyzed using unpaired Student's t-test. *P<0.05.

Figure S3: DGKκ regulates translation and neuronal electrical activity

A) Ribopuromycylation assay in hippocampal neurons. Top panel: no puromycin control. Middle panel: neurons pre-treated with 1.6 mM cycloheximide prior to ribopuromycylation to verify that puromycin signal is translation-specific. Bottom panel: ribopuromycylation signal.

B) Number of active units recorded on MEA chips over time, reflecting neuronal activity from 7 DIV to 35 DIV.

C) Representative raw signal showing action potentials at basal level and during spontaneous bursting activity on a single electrode.

D) Western blot analysis of lysates from WT and *Dgkk*-KO hypothalamic neurons at 7 DIV, showing total and phosphorylated S6 protein. GAPDH was used as a loading control. Quantification: phospho-S6 signal normalized to total S6 and expressed relative to WT. Each dot represents an independent culture. Data are mean ± SEM and analyzed using unpaired Student's t-test. *P < 0.05.

Figure S4: FMRP preferentially binds repetitive, m^6A-modified coding sequences and regulates DGKκ translation

A) IGV representation of *Fmr1* (top panel) and *Rplp0* (bottom panel) mRNAs showing HITS-CLIP-seq profiles of FMRP relative to input.

B) Venn diagram illustrating the overlap between mRNA targets identified in this FMRP CLIP study and targets reported in two independent published datasets (Darnell et al., 2011; Maurin et al., 2018a). Shared and study-specific targets are indicated. For the (Maurin et al., 2018b) CLIP study, the FMRP target list was restricted to mRNAs containing more than one FMRP peak and supported by at least 50 reads.

C) IGV screenshot of FMRP iCLIP-seq data on *Dgkk* mRNA. The red box highlights a WT-specific peak corresponding to a truncation event indicative of an FMRP binding site, as predicted based on iCLIP read-through profiles (Hafner et al., 2010).

D) AlphaFold-predicted structure of human DGKκ, highlighting the intrinsically disordered region corresponding to the EPAP domain.

E) Translation efficiency measurements of the indicated constructs in HeLa cells. Luciferase signals were normalized to RNA levels of the corresponding constructs.

F) qRT-PCR analysis of *Mettl3* expression in cortical neurons treated at DIV5 for 72 h with Accell control siRNA or siRNA targeting *Mettl3*. Fold changes were calculated using the ΔΔCT method with ActB as the housekeeping gene. Data are mean ± SEM and were analyzed using multiple t-tests. ****$P < 0.0001$.

G) qRT-PCR analysis of the indicated genes in cortical neurons treated at DIV5 for 72 h with Accell control siRNA or siRNA targeting *Mettl3*. Fold changes were calculated using the ΔΔCT method with *ActB* as the housekeeping gene. Data are mean ± SEM and analyzed using multiple t-tests comparing expression in siControl and si*Mettl3* conditions for each gene. *$P<0.05$.

H) EMSA using purified human His-tagged FMRP isoform 1 and radiolabeled EPAP RNA probes with or without m^6A modification.

I) IGV representation of *Dgkk* mRNA showing RIP-seq profiles of YTHDF proteins in hippocampal neurons (Flamand and Meyer, 2022).

J) Schematic of the RNA nHU assay used to assess binding of EPAP RNA probes incubated with WT or *Fmr1*-KO neuronal lysates. Probes were incubated with lysates at concentrations ranging from 0 to 2.5 µM. Binding index (BI) values were estimated by non-linear regression fitting.

K) qRT-PCR analysis of cytosolic and nuclear RNA fractions to assess mRNA nuclear export of the indicated genes in WT and *Fmr1*-KO brain tissue. *U2* snRNA was used as a non-exported nuclear control.

L) qRT-PCR analysis of neurite and soma fractions to assess mRNA transport in WT and *Fmr1*-KO cortical neurons. *Gng3* was used as a poorly transported control mRNA and *Col3a1* as a highly neurite-enriched control.

M) qRT-PCR analysis in HeLa cells co-transfected for 24 h with the indicated constructs and control siRNA or siRNA targeting *METTL3*. GAPDH was used as the housekeeping gene. Data are mean ± SEM and analyzed using multiple t-tests comparing expression in siControl and si*METTL3* conditions for each gene. *P<0.05; **P<0.01.

N) Dot blot analysis using an anti-m^6A antibody on 1 µg of poly(A)+ RNA isolated from HeLa cells treated with DMSO or 20 µM STM2457 for 24 h. Methylene blue staining was used as a loading control. Representative western blots of HA-tagged constructs expressed in HeLa cells treated with increasing concentrations of STM2457 for 24 h are shown. GAPDH was used as a loading control.

O) qRT-PCR analysis of Nluc mRNA in HeLa cells transfected for 24 h with control siRNA or siRNA targeting *YTHDF1* or *YTHDF2*. GAPDH was used as the housekeeping gene. Translation efficiency of Nter-DGKκ–NLuc was measured by normalizing luciferase activity

to RNA levels of the corresponding construct. Data are presented as mean ± SEM and analyzed by one-way ANOVA with comparison to the siControl condition. *P < 0.05.

P) Frequency of amino acids encoded by sequences enriched in FMRP HITS-CLIP-seq targets relative to their frequency in the mouse proteome.

Q–R) IGV representations of *Nisch* (Q) and *Set* (R) mRNAs showing HITS-CLIP-seq profiles of FMRP (upper tracks) and m^6A-seq profiles (lower tracks) in neurons, relative to input (Shafik et al., 2021).

Figure 1

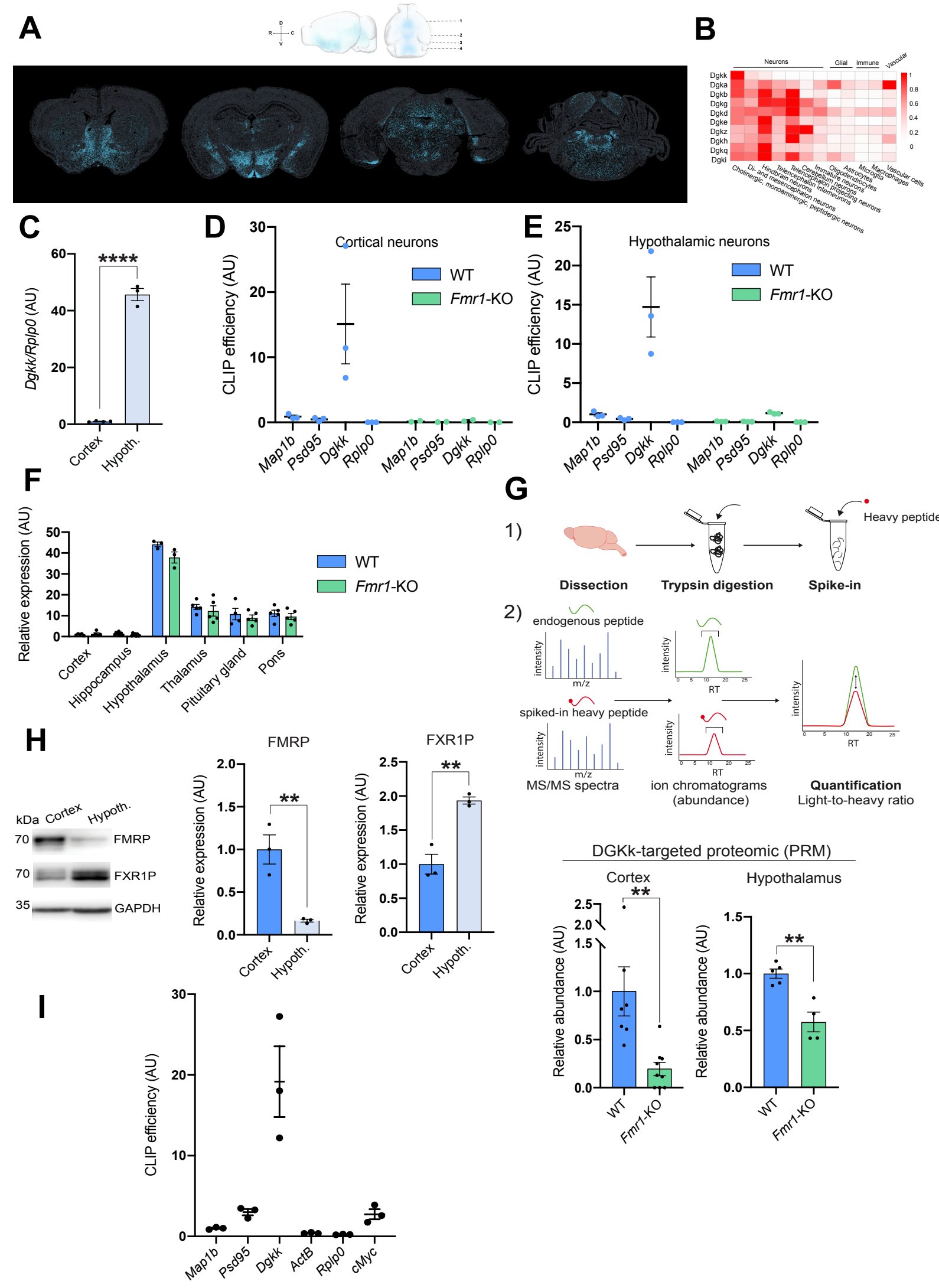
A
B
Neurons
Glial
Immune
Vascular
Dgkk
Dgka
Dgkb
Dgkg
Dgkd
Dgke
Dgkz
Dgkh
Dgkq
Dgki
Cholinergic, monoaminergic, peptidergic neurons
Di- and mesencephalon neurons
Hindbrain neurons
Telencephalon interneurons
Telencephalon projecting neurons
Cerebellum neurons
Immature neurons
Oligodendrocytes
Astrocytes
Microglia
Macrophages
Vascular cells
C
Dgkk/Rplp0 (AU)
****
Cortex
Hypoth.
D
Cortical neurons
CLIP efficiency (AU)
WT
Fmr1-KO
Map1b
Psd95
Dgkk
Rplp0
E
Hypothalamic neurons
F
Relative expression (AU)
Cortex
Hippocampus
Hypothalamus
Thalamus
Pituitary gland
Pons
G
1)
Heavy peptide
Dissection
Trypsin digestion
Spike-in
2)
endogenous peptide
spiked-in heavy peptide
intensity
m/z
RT
MS/MS spectra
ion chromatograms
(abundance)
Quantification
Light-to-heavy ratio
H
kDa
Cortex
Hypoth.
70
FMRP
FXR1P
35
GAPDH
**
I
ActB
cMyc
DGKk-targeted proteomic (PRM)
Relative abundance (AU)

Figure 2

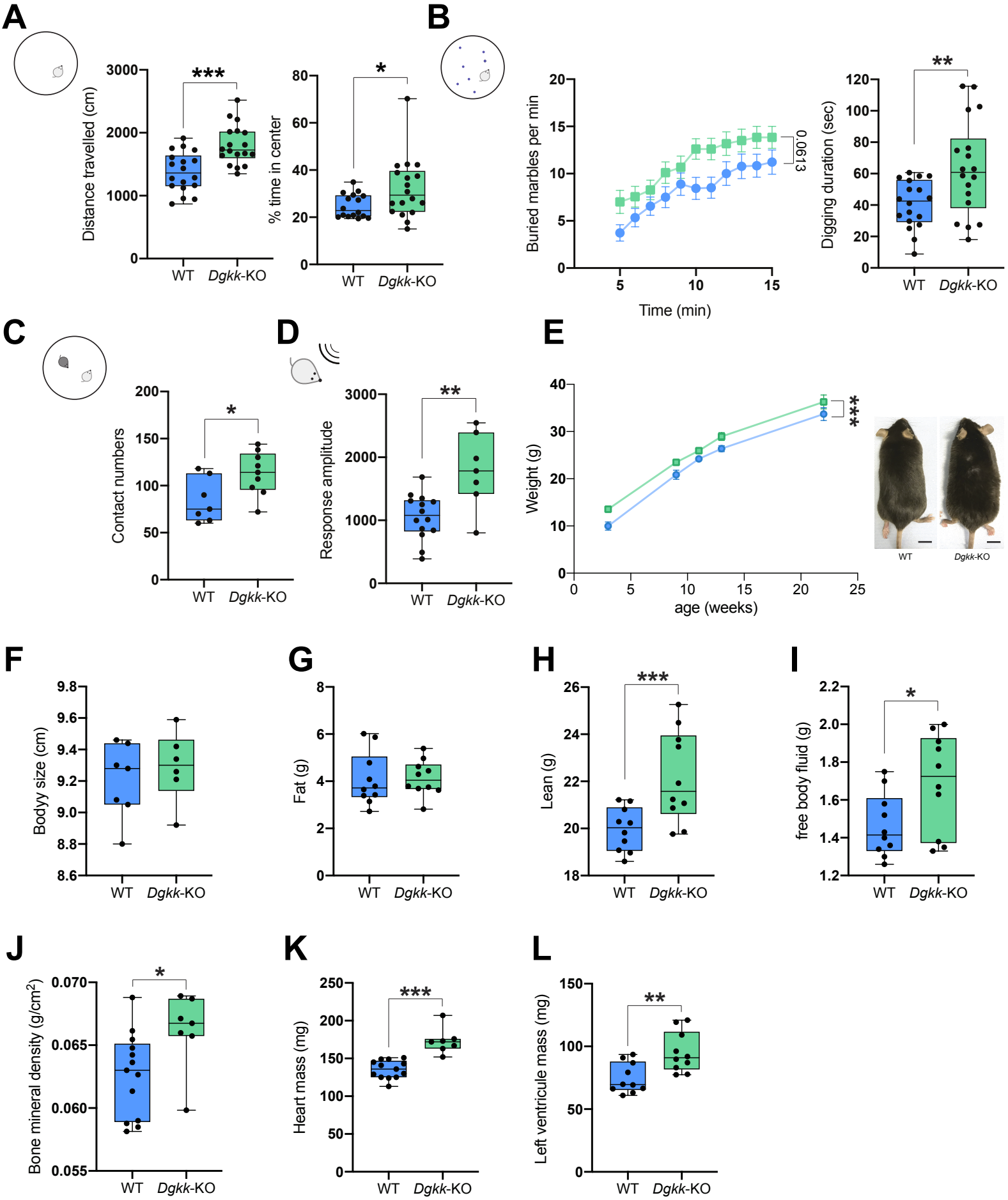
A
Distance travelled (cm)
3000
2000
1000
0
***
WT
Dgkk-KO
% time in center
80
60
40
20
0
*
WT
Dgkk-KO
B
Buried marbles per min
20
15
10
5
0
0.0613
5
10
15
Time (min)
Digging duration (sec)
120
100
80
60
40
20
0
**
WT
Dgkk-KO
C
Contact numbers
200
150
100
50
0
*
WT
Dgkk-KO
D
Response amplitude
3000
2000
1000
0
**
WT
Dgkk-KO
E
Weight (g)
40
30
20
10
0
***
0
5
10
15
20
25
age (weeks)
WT
Dgkk-KO
F
Bodyy size (cm)
9.8
9.6
9.4
9.2
9.0
8.8
8.6
WT
Dgkk-KO
G
Fat (g)
8
6
4
2
0
WT
Dgkk-KO
H
Lean (g)
26
24
22
20
18
***
WT
Dgkk-KO
I
free body fluid (g)
2.2
2.0
1.8
1.6
1.4
1.2
*
WT
Dgkk-KO
J
Bone mineral density (g/cm2)
0.070
0.065
0.060
0.055
*
WT
Dgkk-KO
K
Heart mass (mg)
250
200
150
100
50
0
***
WT
Dgkk-KO
L
Left ventricule mass (mg)
150
100
50
0
**
WT
Dgkk-KO

Figure 3

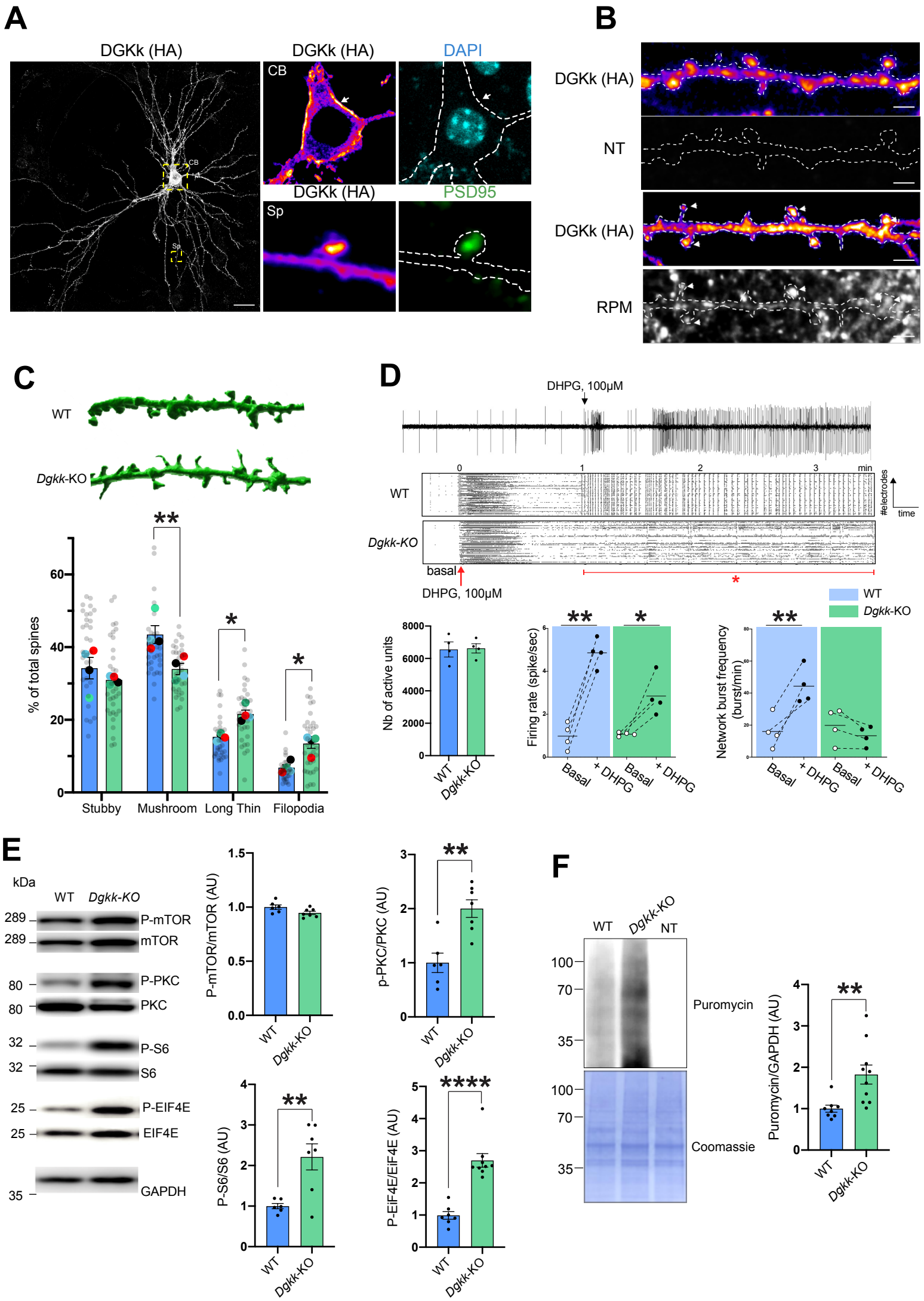
A
DGKk (HA)
DGKk (HA)
DAPI
CB
DGKk (HA)
PSD95
Sp
B
DGKk (HA)
NT
DGKk (HA)
RPM
C
WT
Dgkk-KO
% of total spines
Stubby
Mushroom
Long Thin
Filopodia
D
DHPG, 100µM
WT
Dgkk-KO
basal
DHPG, 100µM
#electrodes
time
Nb of active units
Firing rate (spike/sec)
Network burst frequency (burst/min)
Basal
+ DHPG
E
kDa
WT
Dgkk-KO
P-mTOR
mTOR
P-PKC
PKC
P-S6
S6
P-EIF4E
EIF4E
GAPDH
P-mTOR/mTOR (AU)
p-PKC/PKC (AU)
P-S6/S6 (AU)
P-EiF4E/EiF4E (AU)
F
NT
Puromycin
Coomassie
Puromycin/GAPDH (AU)

Figure 4

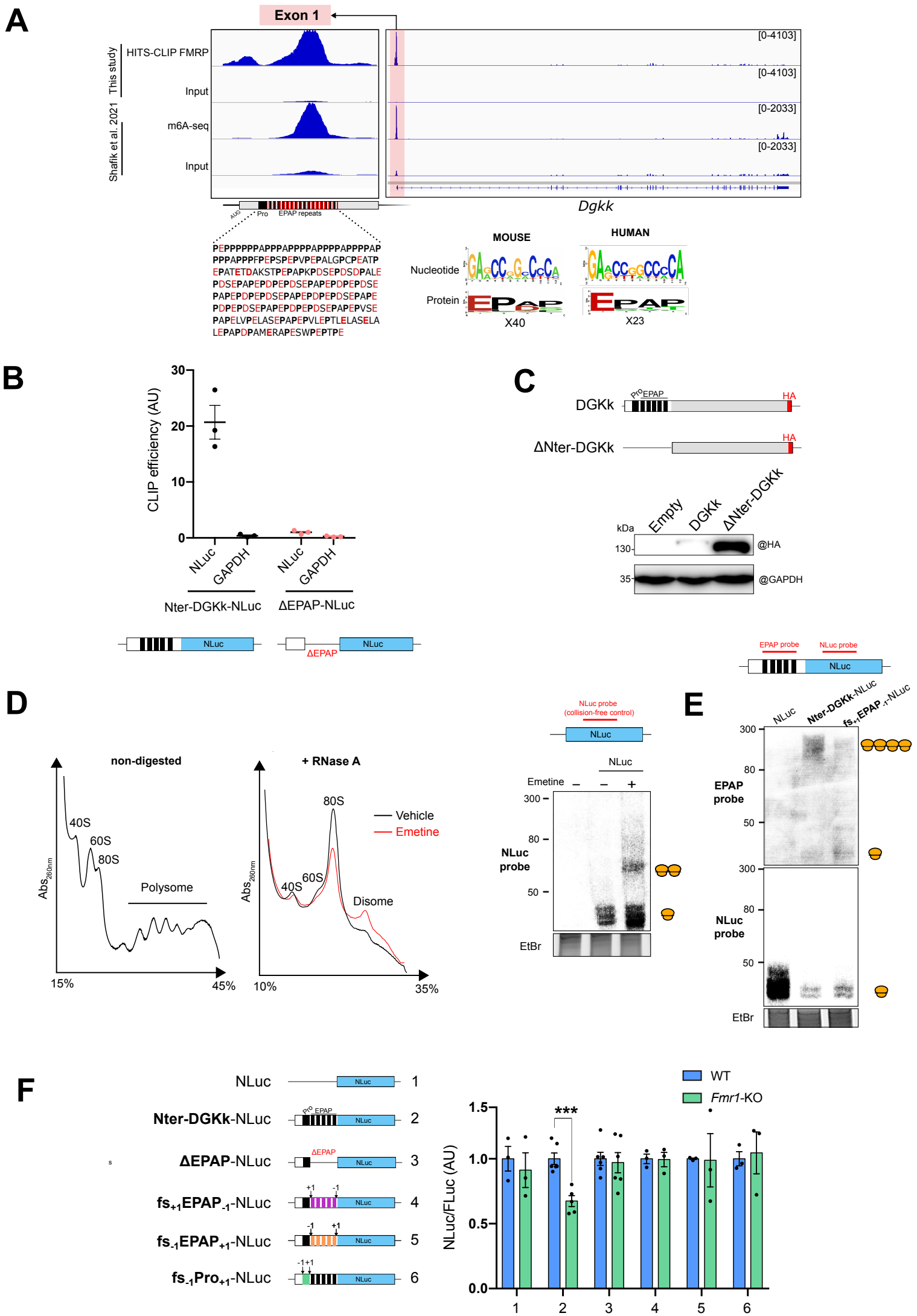
A
Exon 1
This study
HITS-CLIP FMRP
Input
Shafik et al. 2021
m6A-seq
Input
[0-4103]
[0-4103]
[0-2033]
[0-2033]
AUG
Pro
EPAP repeats
Dgkk
PEPPPPPPAPPPAPPPPAPPPPAPPPPAP
PPPAPPPFPEPSPEPVPEPALGPCPEATP
EPATETDAKSTPEPAPKPDSEPDSDPALE
PDSEPAPEPDPEPDSEPAPEPDPEPDSE
PAPEPDPEPDSEPAPEPDPEPDSEPAPE
PDPEPDSEPAPEPDPEPDSEPAPEPVSE
PAPELVPELASEPAPEPVLEPTLELASELA
LEPAPDPAMERAPESWPEPTPE
MOUSE
HUMAN
Nucleotide
Protein
X40
X23
B
CLIP efficiency (AU)
30
20
10
0
NLuc
GAPDH
NLuc
GAPDH
Nter-DGKk-NLuc
ΔEPAP-NLuc
NLuc
ΔEPAP
NLuc
C
DGKk
PRO EPAP
HA
ΔNter-DGKk
HA
Empty
DGKk
ΔNter-DGKk
kDa
130
@HA
35
@GAPDH
D
non-digested
40S
60S
80S
Polysome
Abs260nm
15%
45%
+ RNase A
80S
Vehicle
Emetine
40S
60S
Disome
Abs260nm
10%
35%
NLuc probe
(collision-free control)
NLuc
NLuc
Emetine
–
–
+
300
80
50
NLuc
probe
EtBr
E
EPAP probe
NLuc probe
NLuc
NLuc
Nter-DGKk-NLuc
fs+1EPAP-1-NLuc
300
80
50
EPAP
probe
300
80
50
NLuc
probe
EtBr
F
NLuc
1
Nter-DGKk-NLuc
2
ΔEPAP-NLuc
3
fs+1EPAP-1-NLuc
4
fs-1EPAP+1-NLuc
5
fs-1Pro+1-NLuc
6
WT
Fmr1-KO
***
NLuc/FLuc (AU)
1.5
1.0
0.5
0.0
1
2
3
4
5
6

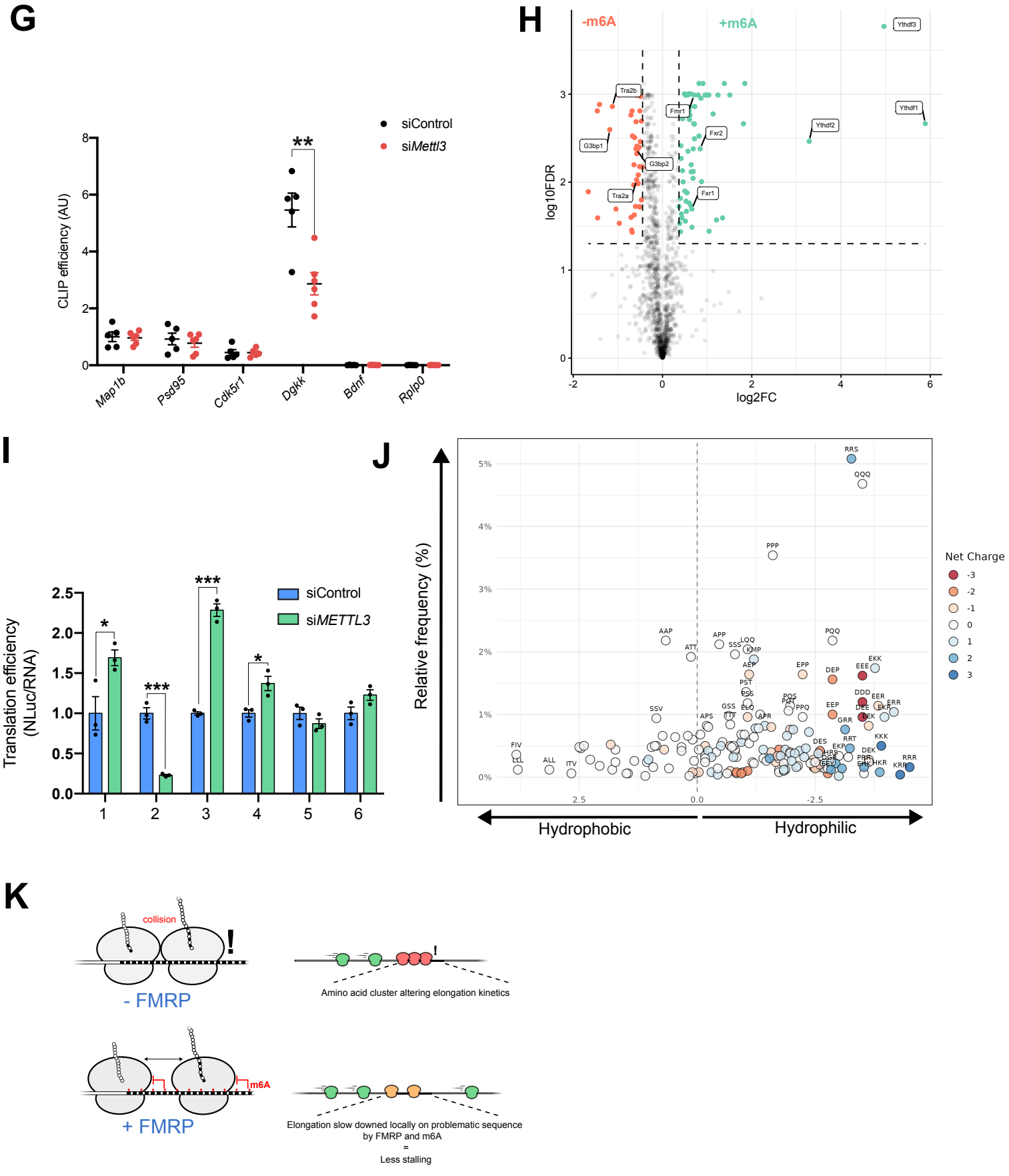
G
siControl
siMettl3
CLIP efficiency (AU)
Map1b
Psd95
Cdk5r1
Dgkk
Bdnf
Rplp0
H
-m6A
+m6A
log10FDR
log2FC
Tra2b
Fmr1
Fxr2
G3bp1
G3bp2
Tra2a
Fxr1
Ythdf3
Ythdf1
Ythdf2
I
siControl
siMETTL3
Translation efficiency (NLuc/RNA)
J
Relative frequency (%)
Net Charge
Hydrophobic
Hydrophilic
K
collision
- FMRP
Amino acid cluster altering elongation kinetics
m6A
+ FMRP
Elongation slow downed locally on problematic sequence
by FMRP and m6A
=
Less stalling